Applied Mechanics

The mechanical behavior of model-scale ice: experiments, numerical modeling and scalability

Rüdiger Ulrich Franz von Bock und Polach

Aalto University

DOCTORAL DISSERTATIONS

Aalto University publication series
DOCTORAL DISSERTATIONS 98/2016

The mechanical behavior of model-scale ice: experiments, numerical modeling and scalability

Rüdiger Ulrich Franz von Bock und Polach

A doctoral dissertation completed for the degree of Doctor of Science (Technology) to be defended, with the permission of the Aalto University School of Engineering, at a public examination held at the lecture hall K1 / 216 of the school on 10th of June, 2016 at 12:00 noon.
This doctoral thesis is conducted under a convention for the joint supervision of thesis at Aalto University (Finland) and the Norwegian University of Science and Technology (Norway)

Aalto University
School of Electrical Engineering
Applied Mechanics
Norwegian University of Science and Technology / Department of Marine Technology

Supervising professors
Professor Pentti Kujala, Aalto University, Finland
Professor Sören Ehlers, Norwegian University of Science and Technology, Norway

Preliminary examiners
Professor Rocky Taylor, Memorial University, Canada
Dr. Richard McKenna, R.F. McKenna Associates, Canada
Professor Robert Ettema, Colorado State University, United States of America

Opponents
Professor Rocky Taylor, Memorial University, Canada
Professor Lennart Josefson, Chalmers University of Technology, Sweden

Aalto University publication series
DOCTORAL DISSERTATIONS 98/2016

ISBN 978-952-60-6822-0 (printed)
ISBN 978-952-60-6823-7 (pdf)
ISSN-L 1799-4934
ISSN 1799-4934 (printed)
ISSN 1799-4942 (pdf)
http://urn.fi/URN:ISBN:978-952-60-6823-7

Unigrafia Oy
Helsinki 2016

Finland

Aalto University

Abstract

Aalto University, P.O. Box 11000, FI-00076 Aalto www.aalto.fi

Author
Rüdiger Ulrich Franz von Bock und Polach

Name of the doctoral dissertation
The mechanical behavior of model-scale ice: experiments, numerical modeling and scalability

Publisher School of Engineering

Unit Applied Mechanics

Series Aalto University publication series DOCTORAL DISSERTATIONS 98/2016

Field of research Arctic Marine Technology

Manuscript submitted 15 June 2015 **Date of the defence** 10 June 2016

Permission to publish granted (date) 29 April 2016 **Language** English

☐ **Monograph** ☒ **Article dissertation** ☐ **Essay dissertation**

Abstract

Increasing levels of transportation and exploratory activities in the High North increase the significance of ice-capable ship designs, and the demand for them. This demand covers a wide range of ship types; such as tugs, vessels for search and rescue (SAR), patrol boats, military vessels, cruise ships, and merchant ships. Both the economically driven preference for operations in the Arctic over operations in a warmer climate, and the safety of the operations, require adequate performance prediction methods. The capability of model-scale ice and its availability and advantages in handling compared to sea ice spurred to the decision to investigate its material behavior to develop a numerical model. This model serves as a cornerstone towards a numerical ice tank and provides insight into the mechanical behavior of model-scale ice. Therefore, systematic ice property tests were conducted with the model-scale ice of Aalto University to define the material behavior. The model-scale ice is fine grained (FG) and doped with ethanol to artificially weaken the material. The experiments investigate the behavior until failure in tension, compression and bending. Furthermore, the elastic modulus is determined by ice sheet deflection experiments and the grain-size is measured. The stress plane that is investigated is orthogonal to the vertical (thickness) coordinate and is the same as the one in which stresses occur when ships interact with ice. On the basis of the experiments, the mechanics and the constitution of the model-scale ice are investigated to define a suitable material model and its parameters. It was found that a damage based elasto-plastic material model represents the behavior of the Aalto model-scale ice well. The numerical model accounts explicitly for flaws in the model-scale ice, comprised of voids filled with liquid and air, which are randomly distributed. It is found that the random distribution of flaws enables the reproduction of the variation in experimentally observed failure patterns and affects the response forces. Furthermore, the cantilever beam bending experiments and their simulation reveal that the gradual change of ice properties over thickness has to be modeled to represent the experimentally measured axial stiffness and flexural stiffness in the same model.
Ultimately, the model-scale ice is demonstrated to be a functionally graded material which is capable of representing tensile, compressive and flexural failure modes.
Additionally, the development of the numerical model of the Aalto model-scale ice provides a deeper insight into its mechanical deformation processes. The material behavior that is found reveals that Cauchy similitude in scaling cannot be applied, because the model-scale ice of Aalto University is on micro scale not a purely elastic material. Consequently, model-scale ice consumes more energy prior to bending failure than a material complying Cauchy similitude.

Keywords Model ice, numerical model, plasticity, bending strength, scaling

ISBN (printed) 978-952-60-6822-0 **ISBN (pdf)** 978-952-60-6823-7

ISSN-L 1799-4934 **ISSN (printed)** 1799-4934 **ISSN (pdf)** 1799-4942

Location of publisher Helsinki **Location of printing** Helsinki **Year** 2016

Pages 168 **urn** http://urn.fi/URN:ISBN:978-952-60-6823-7

Abstract

Increasing levels of transportation and exploratory activities in the High North increase the significance of ice-capable ship designs, and the demand for them. This demand covers a wide range of ship types; such as tugs, vessels for search and rescue (SAR), patrol boats, military vessels, cruise ships, and merchant ships. Both the economically driven preference for operations in the Arctic over operations in a warmer climate, and the safety of the operations, require adequate performance prediction methods.

The capability of model-scale ice and its availability and advantages in handling compared to sea ice spurred to the decision to investigate its material behavior to develop a numerical model. This model serves as a corner-stone towards a numerical ice tank and provides insight into the mechanical behavior of model-scale ice. Therefore, systematic ice property tests were conducted with the model-scale ice of Aalto University to define the material behavior. The model-scale ice is fine grained (FG) and doped with ethanol to artificially weaken the material. The experiments investigate the behavior until failure in tension, compression and bending. Furthermore, the elastic modulus is determined by ice sheet deflection experiments and the grain-size is measured. The stress plane that is investigated is orthogonal to the vertical (thickness) coordinate and is the same as the one in which stresses occur when ships interact with ice. On the basis of the experiments, the mechanics and the constitution of the model-scale ice are investigated to define a suitable material model and its parameters. It was found that a damage based elasto-plastic material model represents the behavior of the Aalto model-scale ice well. The numerical model accounts explicitly for flaws in the model-scale ice, comprised of voids filled with liquid and air, which are randomly distributed. It is found that the random distribution of flaws enables the reproduction of the variation in experimentally observed failure patterns and affects the response forces. Furthermore, the cantilever beam bending experiments and their simulation reveal that the gradual change of ice properties over thickness has to be modeled to represent the experimentally measured axial stiffness and flexural stiffness in the same model. Ultimately, the model-scale ice is demonstrated to be a functionally graded material which is capable of representing tensile, compressive and flexural failure modes.

Additionally, the development of the numerical model of the Aalto model-scale ice provides a deeper insight into its mechanical deformation processes. The material behavior that is found reveals that Cauchy similitude in scaling

cannot be applied, because the model-scale ice of Aalto University is on micro scale not a purely elastic material. Consequently, model-scale ice consumes more energy prior to bending failure than a material complying Cauchy similitude.

Preface

This thesis is part of the idea to develop a tool that supports the design of ships operating in ice. The foundation of this goes back to my studies at TU Berlin, where the lectures on ship theory by Dr.-Ing Stefan Harries and his work with FRIENDSHIP-SYSTEMS have been a powerful source of inspiration.

This thesis was written while serving as laboratory manager of the Aalto Ice Tank and is actively influenced by observations and experience on the job. This also applies for my first (model) ice related project at Hamburgische Schiffbau Versuchsanstalt, HSVA, and I am grateful for the training provided by Dr.-Ing Walter Kühnlein, Jens-Holger Hellmann, Dr.-Ing Karl-Heinz Rupp and Klaus Niederhausen. In this context, I want to thank especially Karl-Ulrich Evers and Peter Jochmann from HSVA, with whom I have been working and cooperating in various contexts from 2004 until now. The mutual support in projects and exchange of knowledge has been an outstanding experience.

Since 2012 I have been a member of the ITTC (International Towing Tank Conference) specialist committee on ice. The work and collaboration with its members has also had a valuable impact on the thesis. Therefore, I wish to express my gratitude to Prof. Akihisa Konno, Topi Leiviskä, Dr. Kirill Sazonov, Victor Westerberg, Dr. Michael Lau, Dr. John Wang, Yanghui Wang, Nils Reimer and Peter Jochmann.

My research work at TKK/ Aalto University and the Norwegian University of Science and Technology, NTNU, had many supporters and inspiring contributors along the way, but I wish to thank especially: Juha Alasoini, Pentti Tukia, Teemu Päivärinta from the Aalto Ice Tank, as well as Prof. Stein-Ove Erikstad and Sandro Erceg (NTNU) and Prof. John Dempsey (Aalto / Clarckson University). I am also grateful for the support of Dr. Daniel Hilding from DYNAmore Nordic AB and his support to model the contact problems in LS-DYNA. I am grateful for the time Dr. G. Timco took to discuss parts

of my research, which led eventually to modeling the through thickness properties on the model ice, which turned out to be a key element of the thesis. Special thanks go to Prof. Jani Romanoff (Aalto), who was of great help at various steps, and to my supervisors Prof. Pentti Kujala (Aalto) and Prof. Sören Ehlers (NTNU). I want to thank Prof. Pentti Kujala for the opportunity to conduct my research jointly with being laboratory manager of the Aalto Ice Tank and for the freedom to steer my research. I am very grateful for the support of Prof. Sören Ehlers and his motivation during the process. I appreciate his faith in my research ideas and the discussions on visions and future research implementations.
I also want to express my gratitude to the pre-examiners of this thesis, Prof. Rocky Taylor, Dr. Richard McKenna and Prof. Ettema for their valuable comments.
Finally, I want to thank the Norwegian Shipowners Foundation and Merenkulun Säätiö for funding my research exchanges between Norway and Finland and also NOTUR and the Norwegian Research Council for the access to supercomputer Vilje to run FE calculations. Additional funding was provided at the end of the thesis by the WINICE project of the Academy of Finland.
Lisäksi haluaisin kiittää vaimoani Aulia tuesta ja kannustuksesta.

Helsinki, April 29, 2016,

Contents

Preface **3**

Contents **5**

List of Publications **9**

Author's Contribution **11**

1. Introduction **19**

1.1 Background 19

1.2 Objectives, Scope and Structure of the Thesis 24

1.3 Limitations 26

2. Ship-Ice Interaction **27**

2.1 Interaction Mechanics and Processes 27

2.1.1 Crushing and Bending Failure 27

2.1.2 Ice Sheet Fracture and Breaking Pattern 28

2.1.3 Shoulder Crushing 29

2.1.4 Behavior of Broken Ice Floes 29

2.2 The Level-Ice Resistance of Ships 30

2.2.1 Level-Ice Resistance and its Components 30

3. Sea Ice and Model-Scale Ice **33**

3.1 The Mechanical Behavior of Sea Ice 33

3.1.1 Tensile Strength 33

3.1.2 Compressive Strength 33

3.1.3 Flexural Strength 35

3.2 Properties of Model-Scale Ice 35

3.2.1 The Model-Scale Ice at Aalto University [PI] 35

3.2.2 Summary of the Mechanical Behavior of Model-Scale Ice in the Context of Sea Ice 36

4. Experiments with Model-Scale Ice [PI, PIII] 39

4.1 Grain Size Measurements ([PI]) 39

4.2 Elastic Modulus [PI, PIII] 40

4.3 Tensile, Compressive and Flexural Experiments [PI] 42

4.4 Measurement Accuracy 43

5. A Numerical Model for Model-Scale Ice [PI, PII, PIII] 47

5.1 The Background of the Numerical Model [PII] 47

5.2 The Numerical Model of Model-Scale Ice [PI, PII] 49

5.2.1 A Functionally Graded Property Model for Cantilever Beam Tests 49

5.2.2 A Model with Constant Properties Through Thickness for Uni-Axial Tests 50

5.2.3 The Material Models in LS-DYNA 51

5.3 Definition of Material Parameters 53

5.3.1 Elastic Modulus 54

5.3.2 Yield Strength 55

5.3.3 The Hardening Modulus 57

5.3.4 The Critical Damage Value 59

5.3.5 The Parameter Fitting Technique 61

5.3.6 Other Constants of the Damage Material 62

5.3.7 The Impact of the Void Density and Distribution 63

5.4 Strains and Strain-Rate Sensitivity 64

5.5 Application of Viscous Theory on Model-Scale Ice in Compression 69

5.6 Summary and Main Findings 71

6. The Scalability of Model-Scale Ice Properties and Model Testing [PIII, PIV] 73

6.1 A Review of the State of the Art Scaling Approach 73

6.2 The Scalability of the Bending Strength [PIV] 75

6.2.1 The Functionally Graded Model 75

6.2.2 The Temperature Variation Though-Thickness 76

6.2.3 A Simplified Numerical Example on the Impact of Different Property Distributions 77

6.3 Scalability in Perspective of the Material Stiffness [PI - PIV] . 78

6.4 The Impact of Experimental Differences on the Scalability . . . 80

7. Concluding Remarks **83**

7.1 Conclusion 83

7.2 Discussion and Future Work 85

A. Tabulated Data of Experiments **91**

B. Material Model Parameters **93**

C. FE Stress Plots **95**

C.1 Functionally Graded Cantilever Beam [PIII] 95

C.2 Numerical Tensile Test with Constant Properties Through-Thickness [PII] 96

C.3 Numerical Compressive Test with Constant Properties Through-Thickness [PII] 97

Errata **101**

Publications **103**

Bibliography **151**

List of Publications

This thesis consists of an overview and of the following publications which are referred to in the text by their Roman numerals.

I Rüdiger U. Franz von Bock und Polach, Sören Ehlers and Pentti Kujala. Model-scale ice - Part A Experiments. *Cold Regions Science and Technology*, Volume 94, Pages 74-81, October 2013.

II Rüdiger U. Franz von Bock und Polach and Sören Ehlers. Model-scale ice - Part B Numerical Model. *Cold Regions Science and Technology*, Volume 94, Pages 53-60, October 2013.

III Rüdiger U. Franz von Bock und Polach. Numerical analysis of the flexural strength of model-scale ice. *Cold Regions Science and Technology*, Volume 118, Pages 91-104, June 2015.

IV Rüdiger U. Franz von Bock und Polach, Sören Ehlers. On the scalability of model scale ice experiments. *Journal of Offshore Mechanics and Arctic Engineering*, Volume 137, Issue 5, Pages 1-11, October 2015.

Author's Contribution

Publication I: "Model-scale ice - Part A Experiments"

The author planned and conducted the experiments, analyzed the measurement data, conducted the FE-analysis and wrote the manuscript. Sören Ehlers assisted in the design of the experiments and, together with Pentti Kujala, contributed valuable comments and suggestions.

Publication II: "Model-scale ice - Part B Numerical Model"

The author did the research on suitable material models and the FE-analysis and wrote the manuscript. Sören Ehlers contributed valuable comments and advices.

Publication III: "Numerical analysis of the flexural strength of model-scale ice"

The author is the sole contributor.

Publication IV: "On the scalability of model scale ice experiments"

The author developed the concept of the paper, conducted full-scale and model-scale measurements, conducted all the numerical simulations and wrote most of the manuscript. Sören Ehlers wrote the manuscript part "A numerical model of Baltic Sea ice" and contributed valuable comments and suggestions

NOTATIONS

Symbols

Roman symbols	**Name**
A	Area
A_g	Crystal type constant (g = granular)
C	Constant (in delayed elastic strain equation)
Ch	Cauchy number
CSMF	Comparitive ship merit factor
CP	Cavitation Pressure
D	Damage value
$\dot{D}$	Damage evolution
E	Elastic (strain) modulus
F	Force
F_B	Buoyancy force
F_e	Elastic force
F_i	Inertial force
F_g	Gravitational force
Fr	Froude number
F_S	Sliding force
L	Length
H	Hardening modulus
H_c	Compressive hardening modulus
H_t	Tensile hardening modulus
I	Areal moment of inertia
K	Bulk modulus

K_I	Stress intensity factor
K_{IC}	Fracture toughness of ice
M	Mass
M_b	Bending moment
R	Universal gas constant (Boltzmann)
R_{br}	Breaking resistance in level ice
R_{rot}	Resistance related to ice floe rotation
R_{sub}	Resistance related ice floe submergence
R_{slide}	Resistance related ice sliding along the hull
R_{imp}	Resistance related to ice floe impact
R_{mov}	Resistance related to ship motions
R_{mov}	Resistance related to clearing the ice
R_i	Ice resistance
Q_g	Activation energy for granular crystal structure
S	Damage resistance parameter
S_{equ}	Effective strain modulus
S_L	Layer stiffness
T	Temperature
VC	Tensor viscosity coefficient
Y	Strain energy release rate
a	Fluid bulk sound speed
b	Width
d	Grain diameter
dc	Critical damage value
$d\lambda$	Plastic consistency parameter (Damage model)
g	Gravitational acceleration
h	Ice thickness, height
k	Elastic foundation
l	Length
q	Exponent
r	Plastic strain
r_d	Damage threshold
s^D	Stress deviator
t	Time
t_d	Damage material constant / exponent

v	Velocity
x	Exponent for ice thickness modification
za	Distance to neutral axis

Greek symbols	**Name**
Δ_{tot}	Total uncertainty
α_T	Temperature dependent constant
ϵ	Strain
ϵ_d	Delayed elastic strain
ϵ_p	Plastic strain
ϵ_v	Secondary creep
$\dot{\epsilon_p}$	Plastic flow
$\dot{\bar{\epsilon}_p}$	Plastic strain-rate
η_P	Propulsion efficiency
$d\lambda$	Plastic consistency parameter
λ	Scaling factor
ν	Poisson ratio
ρ_w	Density (of water)
σ	Stress
σ_H	Hydrostatic stress
σ_b	Flexural strength according to the definition of ITTC
σ_c	Nominal compressive strength
σ_{vM}	von Mises stress
σ_p	Plastic stress
σ_x	Axial stress in x-direction
σ_y	Yield stress
ρ	Density
ρ_w	Fluid density

Abbreviations

Abbreviation	**Name**
Aalto	Aalto University
CFD	Computational Fluid Dynamics
CL	Center line of a ship
EEDI	Energy Efficiency Design Index

EGADS	Ethylene-Glycol-Aliphatic-Detergent-Sugar
FE	Finite Elements
FG	Fine Grained
HSVA	Hamburgische Schiffbau Versuchsanstalt
ITTC	International Towing Tank Conference
IOT	Institute for Ocean Technology
NRC	National Research Council Canada
NSR	Northern Sea Route
NTNU	Norwegian University of Science and Technology
SAR	Search and Rescue
SMF	Ship merit factor
SPH	Smoothed particle hydrodynamics
WL	Water line of a ship

Original Features

Ice model tests are the state-of-the-art method to assess the performance of ships in ice. Semi-empirical formulations for the calculation of the ice resistance of ships are not of general validity, because they are based on regression analysis of the performance of specific ships in specific ice conditions. Therefore, the core of the thesis is dedicated to the development of a numerical model of model-scale ice at Aalto University to gain insight into its mechanical behavior and to set a milestone for future model-scale simulations of ships in ice.

The key feature of this numerical model is its grounding in experimental findings. Ultimately, the findings related to the numerical model are put into perspective with state-of-the-art scaling laws.

The following additional features of the thesis are believed to be original:

1. Systematic experiments are presented in PI including tensile, compressive and flexural specimen tests which are performed in the same ice sheet ensuring coherence between the test results of different experiments. Tensile tests are not covered by the standard ITTC (2002) guideline and the method presented is considered to be sufficiently practical to be applied in other ice tanks as well.

2. The Aalto model-scale ice is found to be a material with a low yield limit. The hardening modulus (i.e., a strain modulus or tangent modulus) which is effective after this point is two orders of magnitude smaller than the elastic modulus (PII).

3. The change of the ice properties through-thickness is found to be of high significance for the mechanical behavior. The commonly assumed homogeneity of the properties of model-scale ice over thickness would not allow tensile, compressive and flexural behavior to be represented in one model (PIII).

4. The numerical model that is presented and validated accounts for the physical structure of the model-scale ice, such as grain-size and the inclusions of air and water. The inclusions and their locations are found to affect response forces and failure patterns, since they act as local stress-concentrators in the model-scale ice (PI, PII).

5. The numerical model of the cantilever beam, where some layers respond elastically and others plastically, can explain the difference between the elastic modulus determined by the deflection of an infinite plate and the effective strain modulus determined by cantilever beam tests. The significant difference in results between the two methods is also observed in other ice tanks over the past three decades (PIII, PIV).

6. Model-scale ice tests and material are to comply with Froude and Cauchy similitude and in addition to this it is postulated that the ratio of the elastic modulus to the bending strength is at least around 2000 ($E/\sigma_b \geq 2000$) as for sea ice. The latter is used as a criterion for the brittleness of the material. The model-scale ice investigated in this thesis complies with the set criterion. However, on a microscopic level the elastic modulus plays a small role compared to the high plasticity in the deformation process of tensile, compressive or bending specimen (PII, PIII). This consequently affects the effective strain modulus in bending, S_{equ}, which causes a large deformation of the cantilever beam as $S_{equ}/\sigma_b \ll 2000$ and on micro-scale a non-compliance with Cauchy similitude, which accounts for elastic forces (PIV).

1. Introduction

1.1 Background

Ships are investments and consequently their economic efficiency plays a key role in design and operation. Merchant vessels reflect this by their revenue, which grows by increasing tonnage and speed while reducing operational and capital costs. Those are reflected in parameters of measure such as the *ship merit factor*, SMF, (Cheng, 1968) or the *comparative ship merit factor*, CSMF (von Bock und Polach et al., 2014). In addition to this, with the introduction of the EEDI (Energy Efficiency Design Index, see International Maritime Organization, 2013) a regulatory aspect is added, demanding an increase in the transport efficiency.

In open water the design process can make use of established methods such computational fluid dynamics, CFD, to optimize the hull shape (e.g., Sames et al., 2011). Design validations by model testing in open water can rely on an environment for which properties are well known. However, for ships in ice established simulation methods are not available. In the pre-design phase, the ice resistance is often determined with semi-empirical formulations that are based on a few physical parameters and regression analysis of experimental results. The way those formulations (e.g., Vance, 1980; Zahn and Philips, 1987; Lindqvist, 1989; Keinonen et al., 1991 and Riska et al., 1998) are derived limits their range of validity. A comparison of different semi-empirical resistance methods, including model-scale tests, in von Bock und Polach et al. (2015) shows the method related spread in transport efficiency. In von Bock und Polach et al. (2015) a transit simulation of ice capable tanker *MT Varzuga* (formerly *MT Uikku*) along the Northern Sea Route, NSR, is presented in which semi-empirical methods over-predict the transport efficiency significantly compared to ice model tests. The prediction of performance in

the design process (e.g., von Bock und Polach et al., 2014) affects the decision making and possible mis-predictions may have severe economic consequences. On the one hand, this emphasizes the significance of ice model tests and on the other hand the need for reliable numerical prediction methods.
In addition to the semi-empirical formulations, physical computational models such as Valanto (2001) exist, which are of limited availability, but show partly good agreement with measurements. Valanto (2001) developed an approach in which the ice is represented by a plate as a boundary condition of a potential flow problem. In the simulations, the ice sheet fails once the principal stress equals the flexural strength of the ice. The contact force between the ice and the ship includes a contact coefficient of empirical origin to artificially reduce forces related to the ice crushing process. The total resistance in Valanto (2001) is a combined result of the theoretical model and the semi-empirical approach of Lindqvist (1989). However, in all cases the actual physical constitution of the ice is simplified by using property values of e.g. flexural strength or compressive strength in the form of macroscopic engineering stresses. This may set additional limits of validity on the available models. Macro-scale refers, in this thesis, to a length scale of the order of magnitude of the ice thickness [1]. Macroscopic stresses refer to forces related to the macroscopic specimen dimensions. Micro-scale applies to size levels below macro-scale, such as grain-size level.

Over the past decades computational methods evolved from triangular-plate bending elements applied on ice cantilever beam bending (Svec et al., 1985) to explicit solvers using cohesive elements (Gürtner, 2009), damage models (Moore et al., 2013) including mesh updating algorithms (Kolari et al., 2009) or smoothed particle hydrodynamics, SPH (Das et al., 2014). The trend in the material models applied has evolved from linear elastic material models (Svec et al., 1985) towards modeling on a micro-scale (McKenna, 1992) and accounting for plasticity (e.g., Kolari, 2007; Gürtner, 2009 and Ehlers and Kujala, 2014).

One of the more complex and advanced models available is that of *MDVL, the Marine Dynamics Virtual Laboratory* at NRC-IOT [2], which is used to simulate the interaction between ice and structures (Derradji-Aouat, 2010). The ice model uses the visco-elastic constitutive law for ice (Derradji-Aouat et al., 2000) and the multi-surface failure criterion of Derradji-Aouat (2003).

[1] This applies on full-scale and model-scale.
[2] National Research Council Canada - Institute for Ocean Technology.

The model incorporates instant elastic, visco-elastic, visco-plastic and deformation behavior resulting from damage. Derradji-Aouat (2010) successfully validated the model against unconfined compressive experiments with different strain-rates (Sinha, 1978a) of cyclic compressive loading tests with moderately confined pressure (Stone et al., 1989). According to Derradji-Aouat (2010), more efforts to perform validation and verification of the MDVL are required. McKenna (1992) presented a model on a micro-scale, i.e. grain-size level, of discrete elements consisting of *soft and hard elements* based on Ashby and Duval (1985) to model transient and steady creep. The model includes spring and spring dashpot elements at the discrete element boundaries to represent the mechanical behavior of the grains. Furthermore, the discretization level of finite elements might require cases to model on a size level of individual grains and flaws to represent the deformation behavior adequately (McKenna, 1992), as is done in this thesis.

The development of a material model for ice or model-scale ice has to follow a similar process as for other materials. In order to gain a good understanding of the material behavior, different specimen tests are required. Kerr and Palmer (1972) stated that the properties of sea ice change over thickness due to the temperature gradient. Consequently, the ice has a certain similarity with composite materials that are functionally graded (see, e.g., Reddy, 2011), and the testing of which requires axial tensile tests and bending tests to assess the axial tensile properties of different layers.

Despite the currently strong role of model-scale ice in the design process of ships, little is known about its mechanical behavior and most of it refers to the mechanical behavior on a macro-scale. This means that, e.g., in cantilever beam tests small displacements and rapid failures are observed, from which perfect elastic-brittle failure behavior is abstracted. In processes where sea ice is impacted with high loading rates and strain-rates $\geq 10^{-3}\mathrm{s}^{-1}$ the material behavior may be considered elastic (Derradji-Aouat, 2003) because viscous effects do not have sufficient time to develop (see, e.g., Sanderson, 1988; Cammaert and Muggeridge, 1988 and Derradji-Aouat, 2010). Strain-rates of this magnitude can occur in ship-ice interaction to which the development of model-scale ice, especially in Finland, is closely related (see, Wilkman, 2014). At lower strain-rates the compressive strength was found to be strain-rate sensitive (e.g., Sinha, 1978a Sanderson, 1988) and both laboratory experiments with fresh water ice and field tests with sea ice contributed to the knowledge of the state of the art. (Sinha, 1983) stated that the compressive behavior of

fresh-water ice is similar to sea ice with respect to its rate sensitivity [3].

As the ice properties play a significant role in ice-ship interaction, they need to be accounted for in scaling from prototype to model. The Froude similitude, i.e. Froude number (Equation 1.1) is to be maintained when inertial forces, F_i, and gravitational forces, F_g, are significant and their ratio needs to be kept in the scaled environment. This may be the case when broken ice is accelerated by the momentum of the ship (see Vance, 1975) and restored by gravitational forces. On the basis of sufficiently high strain-rates ($\geq 10^{-}3$), the ice responds with elastic deformations (Derradji-Aouat, 2010) and breaks rapidly, which requires maintaining the Cauchy number as a ratio of inertial forces and elastic forces, F_e (Equation 1.2, Vance, 1975; Schwarz, 1977 and Zufelt and Ettema, 1996 and Section 6.1).

$$Fr = \frac{F_i}{F_g} = \frac{v}{\sqrt{gL}} \tag{1.1}$$

$$Ch = \frac{F_i}{F_e} = \frac{\rho v^2}{E} \tag{1.2}$$

Froude (Equation 1.1) and Cauchy (Equation 1.2) similitude are applied by default in ice model testing and considered appropriate for ice-ship interaction, however the validity of their application may not always be appropriate when the forces, F_i, F_g and / or F_e, play a minor role (Atkins and Caddell, 1974; Atkins, 1975; Schwarz, 1977; Palmer et al., 2009 and Jordaan et al., 2012). An alternative approach of Atkins and Caddell (1974) is based on the consideration that ice contains pre-existing cracks, e.g. air bubbles. The stiffness of the ice sheet changes when the cracks start to grow. Atkins (1975) named the failure force of the cantilever beam *cracking force* and linked it to the fracture toughness (Equation 1.3). Consequently, Atkins (1975) presented a non-dimensional ice number as scaling similitude which combines the Cauchy number and the effects of a defective cracked continuum (Equation 1.3). Equation 1.3 contains the fracture toughness, K_{IC}, length, L, elastic modulus, E, velocity, v, ice density, ρ, and the stress intensity factor, K_I.

$$\begin{aligned} I_n &= Ch^2 \sqrt{\tfrac{EL}{K_{IC}}} \\ &= \tfrac{v^2 \rho \sqrt{L}}{K_I} \end{aligned} \tag{1.3}$$

With reference to the small significance of inertial forces at slow interaction speeds Palmer et al. (2009) promoted to abandon Froude-scaling (Equation

[3] This topic is further addressed in Section 3.1.2.

1.1) and to introduce the application of a dimensionless number based on non-linear fracture mechanics. Another scaling method is presented by Jordaan et al. (2012) which is based on the weakest link theory of Weibull (1939). The consideration of applying the Weibull modulus for scaling is similar to Atkins and Caddell (1974) as it refers to pre-existing flaws in the ice.
The three alternative approaches of Atkins (1975); Palmer et al. (2009) and Jordaan et al. (2012) are not implemented in the standard guidelines of the ITTC (2002). Additionally, their applicability in practice might be limited as even the experimental determination of the fracture toughness for small-scale laboratory tests is still a *"research question"* (Palmer et al., 2009), as well as the practical scaling of flaw sizes (Jordaan et al., 2012). Model-scale ice is artificially doped to adjust the macroscopic strength properties for bending failure and to comply with the target scaling similitudes. Timco (1981a) conducted bending strength measurements with different ice dopants such as various salts, alcohols and sugars. Therefore it is concluded that a combination of low molecular weight and high molecular weight chemicals would be optimal (Timco, 1981a). However, Table 1.1 shows that ice tanks of today operate with model ice types that differ in grain structure and dopant.

Table 1.1. Model ice types in operating ice tanks.

Facility	Country	Grain structure	Chemical dopant
Aalto University	Finland	Fine-grained	Ethanol
Aker Arctic	Finland	Fine-grained	Natrium-chloride
HSVA	Germany	Columnar	Natrium-chloride
Krylov State Research Centre	Russia	Fine-grained / Columnar	Natrium-chloride
National Maritime Research Institute	Japan	Columnar	Propylene Glycol
OCRE / NRC [a]	Canada	Columnar	EGADS [b]

[a] National Research Council - Ocean, Coastal and River Engineering
[b] Ethylene-Glycol-Aliphatic-Detergent-Sugar

The grain structure and the dopant have an impact on the mechanical behavior and the scalability. Schwarz (1985) stated that carbimide model ice has a ratio of compressive strength to flexural strength between two and three which is claimed to be in compliance with sea ice, whereas the fine-grained

model ice, at that time, had a ratio of one. As the elastic forces are considered significant in the deformation process of ice, Schwarz (1977) postulated that in model ice the ratio of the elastic modulus, E, to the flexural strength, σ_b, has to follow Equation 1.4 in analogy to sea ice.

$$\frac{E}{\sigma_b} \geq 2000 \tag{1.4}$$

Both Evers and Jochman (1993)(HSVA) and Jalonen and Ilves (1990)(Aalto) reported plasticity in previous versions of the model ice of their affiliated ice tanks. In addition to this, different experimental methods to determine the elastic modulus yielded substantially different results (Enkvist and Mäkinen, 1984; Evers and Jochman, 1993). The elastic modulus determined by plate bending in Enkvist and Mäkinen (1984) was twice as large as the one determined by cantilever beam tests. It is however unclear, whether encountered differences are related to experimental differences or different material behavior.

The bending strength is the commonly used strength parameter of model ice for which the ITTC (2002) provides recommended procedures and guidelines for physical testing and analysis methods. In both model-scale (e.g. ITTC, 2002) and full-scale (e.g., Anderson and Weeks, 1958; Suominen et al., 2013) the material is assumed to be homogeneous and isotropic with its neutral axis at its center. However, as the temperature distribution through the thickness of sea ice varies, its mechanical properties vary as well (see, e.g., Kerr and Palmer, 1972; Åse, 2013). This applies to model-scale ice as well, where the gradient is likely to be different as the boundary conditions are different as well. Furthermore, Timco (1981a) observed in experiments with various unseeded ices with different dopants that the top-layer appears to be significantly stronger compared to the rest. This complies with operational experience in the Aalto ice tank and suggests that mechanical properties vary through thickness. In model-scale experiments the bending strength is usually determined by in-situ cantilever beam tests, whereas in full-scale cantilever beam tests (e.g. Krupina and Kubyshkin, 2007) three-point bending tests (Suominen et al., 2013, ex situ) or four-point bending tests (Kujala et al., 1990) are conducted. In cantilever beam tests the stress concentrations at the root corners act as stress amplifiers which reduces the tolerable load (see, Svec et al., 1985). Consequently, the though-thickness property distribution, the test type and the mechanical behavior of the material affect the scalability, but to a not yet quantified magnitude.

In order to investigate the mechanical behavior and resulting scalability of the model-scale ice at Aalto University, systematic ice property measurements are conducted and a numerical model is developed. The numerical model is defined on micro-scale with the purpose to reproduce the tensile, compressive and flexural experiments on macro-scale. Furthermore, an assessment of the scalability of model-scale ice is made, based on the insight gained into the mechanics of model-scale ice. Additionally, the thesis provides a review of forces involved in ship-ice interaction and a brief abstract on the mechanical behavior of ice.

1.2 Objectives, Scope and Structure of the Thesis

A numerical model of model-scale ice is to be developed that is in close agreement with the experimental evidence. The scope is, to set a first milestone for a future numerical model-scale testing environment, as well as to contribute to the clarification of the mechanical constitution of the model-scale ice. The primary application of the numerical model-testing environment is to investigate ship interaction with ice, for which physical model scale ice was originally developed. A numerical model of ice that can represent ship-ice interaction processes requires an accurate definition supported by experiments. Therefore, the scope of the publications PI, PII and PIII is to conduct systematic measurements of the failure mechanisms of the Aalto model-scale ice, to define the mechanics of the material and to derive a numerical simulation model that can represent the failure in tension, compression and bending, while accounting for the actual physical constitution of the model-scale ice. This requires all experimentally determined parameters to be represented in the numerical model.
The numerical model should preferably make use of existing models that are already incorporated into finite element-programs to make its use easier for the community. The findings related to the numerical model are to be applied to investigate the scalability of the Aalto model-scale ice with respect to its mechanical behavior in the context of state-of-the-art scaling laws (PIV).

The thesis is based on four journal publication, which are graphically represented in Figure 1.1.

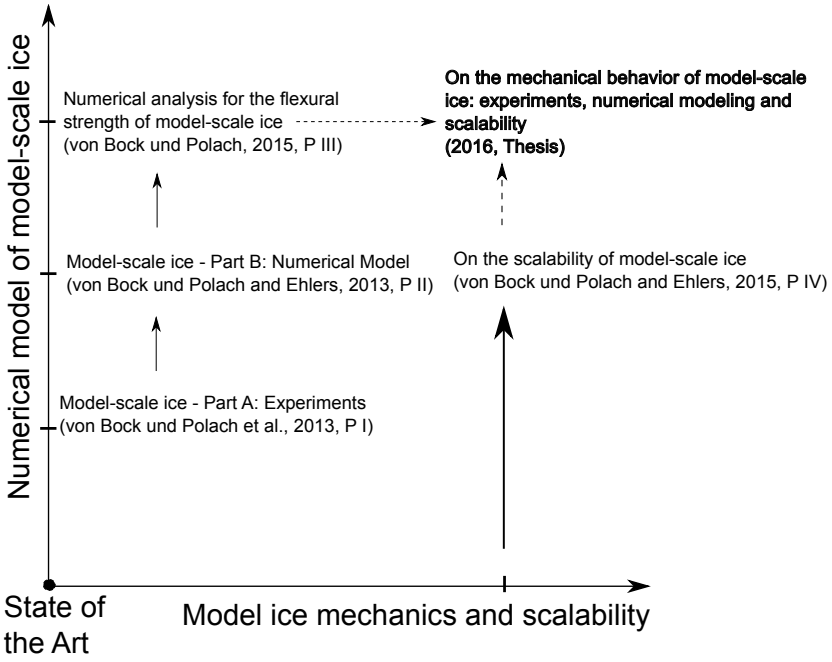

Figure 1.1. Position of the thesis in context with the publications.

1.3 Limitations

The publications PI, PII and PIII present the numerical model of model-scale ice at Aalto University; the publication PIV refers to the scalability of the model-scale ice at Aalto University. The limitations of the thesis are considered to be as follows:

1. The ice property tests conducted in PI are of small sets in terms of statistical analyses with seven to nine specimens. However, the number of samples in ice property testing is small in general, due to time limitations. The sample size reflects the upper standard-threshold of tests in one location in the field of model ice testing [4].

2. All experiments are conducted at a single loading rate of 6 mm/s for which specimens fail within less than one second. Earlier conducted uni-axial tension and compression tests did not reveal loading rate sensitivity in the range from 1 mm/s to 16 mm/s; consequently, strain-rate sensitivity is not considered in this thesis. This automatically limits the validity of the presented model to interactions that are comparable to a ship model breaking model-scale ice.

3. The defined numerical model (PII) and its parameters can represent the

[4]Best practice in daily ice tank tests are three to four samples per location.

failure in tension, compression and downward bending under uni-axial loading. It is not (yet) suitable for engineering applications such as actual ship-ice interaction due to excessive computational costs. The calculation of larger ice sheets is currently infeasible because of memory limitations.

4. The material model according to Lemaitre and Desmorat (1992) is based on von Mises stresses, which cannot distinguish between tensile and compressive stresses. In consequence the compressive and tensile layers in the cantilever beam model are to be defined a priori.

5. Compressive tests in other ice sheets indicate an increase of the nominal pressure with decreasing impact surface (PIV). The model presented in PII cannot represent this effect; additionally, the physical cause has also not yet been identified.

2. Ship-Ice Interaction

This chapter describes ice mechanics involved in ship-ice interaction and indicates the most significant parameters affecting the process. The flexural strength, respectively the failure in bending, plays a significant role for the resistance of ships and is, consequently, scaled to model-scale. Therefore, the numerical model this thesis presents focuses on the flexural failure of model ice and the processes it involves.

2.1 Interaction Mechanics and Processes

This section describes qualitatively the processes involved when a ship proceeds through ice in the chronological sequence of the process steps. Thereafter, the breaking pattern and also the process of the ice sliding along the hull is briefly introduced.

2.1.1 Crushing and Bending Failure

The crushing and bending failure are demonstrated in a 2D cross-section plane at the longitudinal centerline of the ship. At the first contact between the inclined hull and the ice the normal force, F_N, causes highly localized compressive loads at the ice edge, which causes so-called crushing failure of the ice (Enkvist et al., 1979, Figure 2.1). At the same time the vertical force, $F_V = F_N \cos\phi$, as a function of the normal force and the stem angle, ϕ, bends the ice sheet downwards [1]. The crushing continues until the maximum crushing depth ξ_c is reached. The downward bending continues until the flexural strength of the ice sheet is reached and it breaks.
The bent ice sheet fails by exceeding the tensile strength on the top surface. The horizontal forces, F_H, introduce compressive stresses in the top

[1] According to Varsta (1983) the friction in the ship-ice contact surface is small and can be neglected.

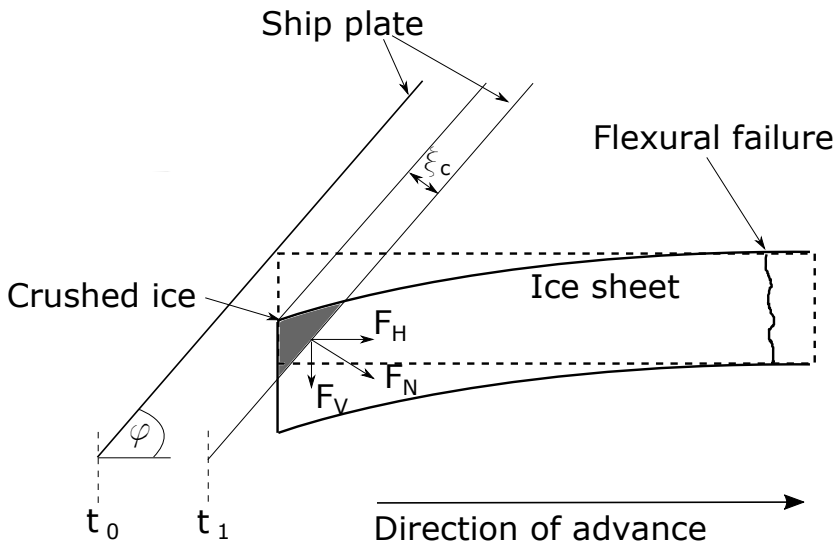

Figure 2.1. Schematic 2D description of the crushing and bending failure, with a horizontal direction of advance and the time instance t_0 prior to contact and t_1 when the crushing process terminates and the ice sheet fails. The crushing depth is ξ_c. The Figure is based on Varsta (1983).

layer which are superimposed to the tensile bending stresses and can delay the flexural failure (Valanto, 1997; Vance, 1975).

2.1.2 Ice Sheet Fracture and Breaking Pattern

The interaction between ice and ship can form radial cracks and circular cracks, which are illustrated in Figure 2.2. The radial cracks originate from the bow of the ship, which may act in a similar fashion as a horizontal indenter. The ship introduces compressive stresses in the near field and, in reaction, causes tensile stresses to build up in the far field (Sanderson, 1988). The occurring stress intensity factor, K_I, at the impact zone depends on far-field tensile forces which are a function of the compressive load introduced by the ship (Sanderson, 1988). Once K_I reaches the fracture toughness of the sea ice, K_{IC}, radial cracks start to form (Palmer et al., 1983; Sanderson, 1988).
The circular cracks in the ice sheet originate from the flexural failure after bending(see Figure 2.1) and proceed parallel to the initial edge and create cusps. Goldstein and Osipenko (1993) describes the crack-growth stability as a result of the in-plane compression (see also Valanto (1997)) and the acting bending moment introduced by the ship. Consequently, the forces related to the downward bending and the flexural strength of the ice sheet determine how cusps break.
As illustrated in Kärmäräinen (1993) (based on observations from E. Mäkinen,

1976, in full-scale) the breaking pattern in level-ice does not necessarily include radial cracks, which applies also on model-scale ice, (Ettema et al., 1989; Yamaguchi et al., 1997, 1999) as the required condition on the stress intensity is not fulfilled. Valanto (2001) refers to one radial crack as an extension of the center line, CL (Figure 2.2), while Vance (1975) referred to several originating from the stem.

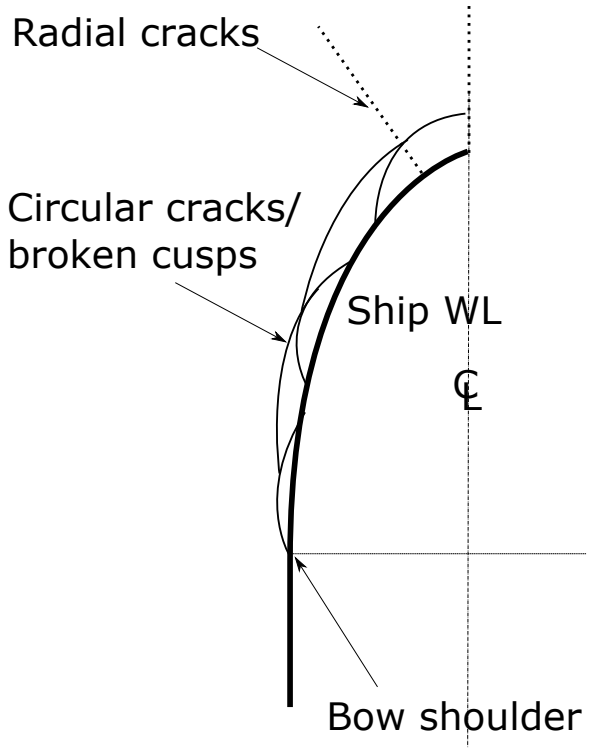

Figure 2.2. Schematic breaking pattern with circular and radial cracks, based on illustrations in (Vance, 1975; Palmer et al., 1983; Ettema et al., 1989; Kärmäräinen, 1993; Valanto, 2001) on the water line, WL, level of a ship.

2.1.3 Shoulder Crushing

In case the width of the broken ice field is smaller than the width of the vessel, as indicated in Figure 2.2, the bow shoulder may compressively interact with the ice by crushing it, so called shoulder crushing (Kujala and Riska, 2010; Riska, 2010). This interaction may also occur with broken wedges that do not submerge or turn before the bow shoulder approaches. The occurrence of shoulder crushing can cause an increase of resistance (e.g. Su et al., 2010).

2.1.4 Behavior of Broken Ice Floes

Ice floes that are bent sufficiently so that occurring stresses exceed the bending strength, break off the ice sheet and proceed along the hull (Figure 2.3). Directly after breaking, the floe rotates with a relatively steady speed (Valanto, 2001). The top surface of the floe, which is in step 2 and 3 in contact with the ship, may be fully [2] or partly ventilated. Full ventilation is more likely to occur at higher speeds, than at lower speeds (Valanto, 2001). After the rotation and submergence the floe impacts the proceeding ship in step 2 and proceeds by sliding along the hull in step 3. In the sliding process the full ventilated floes produce a sliding resistance force, F_S, resulting from the buoyancy force, F_B, and the friction coefficient between the hull and the ice. In case that full ventilation does not occur, the pressure field in the gap between hull and ice floe may affect the resistance (Valanto, 2001; Kärmäräinen, 2007). In Figure 2.3 this process is illustrated for the bow stem, but occurs in a similar fashion also in other hull areas (e.g., Kujala and Riska, 2010).

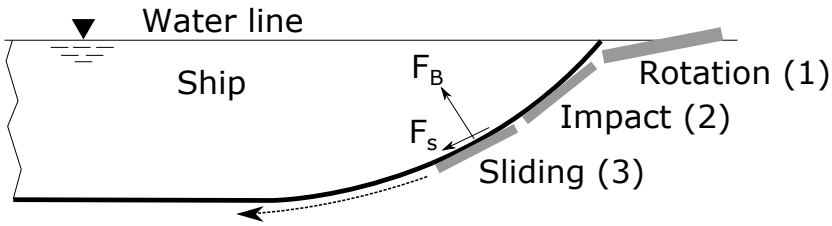

Figure 2.3. Progress of ice floes after being broken off at the bow stem from the intact ice sheet in a 2D view.

2.2 The Level-Ice Resistance of Ships

2.2.1 Level-Ice Resistance and its Components

The ice resistance represents the sum of horizontal response forces due to the ship-ice interaction described in Section 2.1.

Equation 2.1 shows the component break down according to Vance (1975). The ice resistance is defined as sum of the breaking resistance, R_b, the resistance related to the rotation of the ice floe, R_{rot}, the resistance due to ice floe submersion, R_{sub}, the resistance caused by the relative sliding of ice against the hull, R_{slide}, resistance due to ship motions, R_{mov}, resistance to impacts

[2] Ventilated means free of water.

between hull and ice, R_{imp} (see Figure 2.3), and the resistance from clearing the ice, respectively *"pushing the ice away"* (Vance, 1975), R_{clear}.

$$R_i = R_b + R_{rot} + R_{sub} + R_{slide} + R_{mov} + R_{imp} + R_{clear} \tag{2.1}$$

The breaking down of the components may vary from author to author as some do not account for all components and others may see some smaller components as a part of other components. A component breakdown according to Ettema et al. (1989), is similar to Equation 2.1. The ice resistance is divided into icebreaking (R_b), the submergence and displacement of broken ice, including the momentum exchange to it ($R_{sub} + R_{rot} + R_{imp}$), and the resistance due to ice floes sliding along the hull R_{slide} as well as due to ship motions R_{mov}. The impact of ship motions is of higher significance at lower speeds and / or thicker ice, but not at higher ship speeds or thinner ice (e.g. Enkvist (1972); Ettema et al. (1987); von Bock und Polach and Ehlers (2011)) consequently, the significance of this part is case dependent.
A more condensed break down of components is found in Equation 2.2 after Myland and Ehlers (2014) or in Enkvist (1983), who summarized the ice resistance as breaking resistance, submersion resistance and velocity resistance.

$$R_i = R_b + R_{rot} + R_{sub} + R_{slide} \tag{2.2}$$

The force created by ice floes sliding along the hull is R_{slide}. This force depends on the friction coefficient between hull and ice when the ice floe is fully ventilated (dry friction). Otherwise, when water is entrapped between floe and hull R_{slide} depends on the pressures in the gap between hull and floe (see, Kärmäräinen, 2007 and Section 2.1.4. This resistance increases with speed (Lindqvist, 1989; Valanto, 2001; Riska, 2010) and is considered mainly causative for the speed dependency of the ice resistance (see also Kärmäräinen, 1993).
The resistance increase due to the ice floe or ice cusp rotation after breaking is R_{rot}, in sequence of which the remaining energy introduced into the ice floe causes it to submerge, which is R_{sub}. According to Kujala and Riska (2010) the required energy expenditure of the ship for turning the ice floe is small. The breaking resistance, R_b, resembles forces related to crushing, downward bending and subsequent flexural failure (Section 2.1) and fracturing (Section 2.1.2). The latter is usually not explicitly considered. The icebreaking resistance is the largest resistance component of the ice resistance (e.g. Ettema et al., 1989; Riska, 2010; Kujala and Riska, 2010) of which the flexural failure is the most significant (see, e.g. Ettema et al., 1989). Enkvist (1983) stated that flexural failure contributes between 40 % - 80 % (see i.a. Poznyak and

Ionov, 1981; Nyman, 1986 of the total resistance [3] in full-scale and model-scale. Schwarz (1977) quantified the fraction of icebreaking by 30 % - 70 % of the ice resistance.

In model-scale test series at the Aalto Ice Tank, the ice-breaking resistance of the ice-going tanker Uikku was found to be 60% - 70% (von Bock und Polach (2010)). The fraction is determined by resistance tests in level-ice and pre-sawn ice. In the pre-sawn ice condition the contribution of flexural failure is eliminated, but it is not certain to what extend crushing interaction might be eliminated.

The icebreaking resistance holds, in many cases, the largest fraction of the entire ice resistance. Independent from the degree of detail of the component breakdown (Equation 2.1 and Equation 2.2) the compressive edge crushing and the flexural failure of the ice sheet are commonly considered the most relevant contributors to the ice resistance involving ice mechanics. The breaking related to flexural failure is for the ship-ice interaction the more significant one (e.g. Kujala and Riska, 2010) and is, consequently, the one scaled and modeled in model-scale tests (ITTC, 2002). This is also reflected in semi-empirical formulas for the ice resistance (see, e.g., Lindqvist, 1989), where the flexural strength, σ_b, is usually the only accounted ice property [4].

An analysis of the maximum forces experienced by the vessels *Oden* and *Polar Sea* revealed that the loads in ramming events (*Polar Sea*) can be represented by methods based on local high pressures. However, when the ice failure is dominated by flexure (in case of *Oden*) the maximum force had to be represented by a model based on the flexural strength of sea ice (Jordaan, 2001).

The currently established method of ice model-scale testing is designed on the basis of ships moving in level ice and modeling relevant parameters, which is generally acknowledged (e.g. Jordaan et al., 2012). Riska et al. (1994) demonstrated a good correlation of the level ice resistance prediction based on model tests (at Aalto Ice Tank) compared to full-scale tests for some conditions, whereas in others cases there was less agreement. This may be due to the fact that not all resistance components can be scaled in the same way (Grochowalski and Hermanski, 2011) or that the magnitude of certain resistance parts might not be proportional in model-scale and full-scale Vance (1975).

[3] The total resistance is a superposition of the ice resistance and the open water resistance, i.e. the percentage of ice breaking of the ice resistance is even larger.

[4] It is acknowledged that the flexural strength is not an actual ice property, but it is often named as such.

3. Sea Ice and Model-Scale Ice

This section describes the mechanics of sea ice and model-scale ice and ranks them. The mechanics of model-scale ice uses findings presented in the papers related to this thesis (PI, PII, PIII, PIV). The review is reduced to the mechanical behavior in tension, compression and bending as these are the researched aspects in this thesis in model-scale. The high strain-rates in ship-ice interactions allow its idealization as a linear elastic material Derradji-Aouat, 2010. Model-scale ice was initially developed to assess the performance of ship models in ice (see, e.g., Enkvist, 1990). The first design of a model testing basin in Finland refers to the transport of oil through the Canadian Arctic Islands by ship and the assessment of its resistance (Wilkman et al., 2010). Consequently, there is a strong emphasis on the flexural strength of ice as it predominantly fails against ships in bending (see Chapter 2).

3.1 The Mechanical Behavior of Sea Ice

3.1.1 Tensile Strength

The tensile strength is mainly affected by the porosity and temperature (Timco and Weeks, 2010). Experiments with different strain-rates presented by Richter-Menge and Jones (1993) indicated that the strain-rate sensitivity between rates of $10^{-5}\mathrm{s}^{-1}$ and $10^{-3}\mathrm{s}^{-1}$ is small. Consequently, according to Timco and Weeks (2010), the strain-rate effect in tension can be neglected and the tensile strength can sufficiently be presented as a function of porosity.

3.1.2 Compressive Strength

The compressive behavior is here classified into deformations at low strain-rates, where viscosity plays a role, and deformations at higher strain-rates, where the effect of pressure localizations (e.g. Johnston et al., 1998; Jordaan et al., 1999; Dempsey et al., 2001; Jordaan, 2001; R.S. and I.J., 2015) may be encountered in the ice-structure interface, which is found as so called *pressure-area relationship* in design references (19906, 2010; Ehlers et al., 2015) [1].

In contrast to tensile loading the compressive stress can experience a significant loading rate or strain-rate sensitivity (Hawkes and Mellor, 1972; Karr and Das, 1983).

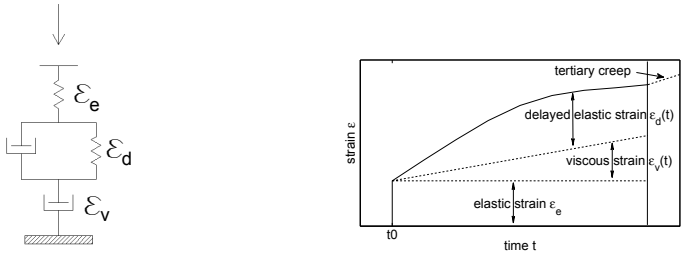

a Representation of the ice rheology with mechanical elements

b Qualitative representation of the strain development in ice over time

Figure 3.1. strain-rate dependent deformation of ice, reproduced according to Sanderson (1988).

In the case that strain-rates are sufficiently low to trigger viscous effects, the total strain is reassembled by elastic, ϵ_e, viscous ϵ_v, and delayed elastic strain, ϵ_d which is shown in Figure 3.1a and Figure 3.1b. Furthermore, the contribution of the different strain components changes over time (Figure 3.1b).
The progress of the delayed elastic strain is defined as an exponential function in compliance with experiments (Sinha, 1978a, 1982, 1983) as a function of the elastic modulus, the grain diameter and time. The non-recoverable deformation ($\epsilon_v(t)$) in Figure 3.1b is named secondary creep (Sanderson, 1988; Schulson and Duval, 2009). The secondary creep strain-rate $\dot{\epsilon_v}(t)$ can also be expressed as an exponential function depending on temperature and crystal structure (see, e.g., Glen, 1955; Shoji and Higashi, 1978). At the end of primary and secondary creep tertiary creep commences (see Figure 3.1b) which is associated with the formation of micro-cracks at grain boundaries (Sanderson,

[1] Pressure-relationship can be associated with crushing failure

1988). Those micro-cracks might coalesce with increasing strain and accelerate deformation; however recrystallization processes might also play a role here (Sanderson, 1988). The inelastic strain of ice may be up to ten times larger than the elastic strain (Le Gac and Duval, 1979). Equations and additional discussion on viscosity and its application on model-scale ice is found in Section 5.5 and the Discussion in Section 7.2.

3.1.3 Flexural Strength

The flexural strength is not typically considered as a material parameter since in bending the acting stresses are tensile and compressive. Nevertheless, it is an important parameter of high practical relevance in ship-ice interaction as ice predominantly fails in bending. The behavior in short loadings in ice sheet deflection, i.e. high strain-rates, causes mainly elastic strain (Weeks and Assur, 1967; Derradji-Aouat, 2003) as time dependent terms do not have enough time to develop (Jordaan, 2001; Derradji-Aouat, 2010). The threshold for these high strain-rates, $\dot{\epsilon}$, in which ice behaves brittlely is around $\dot{\epsilon} \geq 10^{-3}$ s^{-1}, where it may be modeled linear-elastically (Derradji-Aouat, 2003). Furthermore, the bending strength is incorporated in most semi-empirical ice resistance calculation methods (see, e.g., Lindqvist, 1989). Timco and Weeks (2010) summarized that the flexural strength can be expressed as a function of porosity, as loading rate effects and, in consequence, strain-rate effects are considered of minor significance. This indicates the significance of tensile properties in flexural failure as those are likewise considered strain-rate independent compared to compressive properties.

3.2 Properties of Model-Scale Ice

3.2.1 The Model-Scale Ice at Aalto University [PI]

The Aalto Ice Tank has a lateral area of 40 m x 40 m, with a uniform depth of 2.8 m (see Figure 3.2). The model-scale ice is fine-grained (FG), as it is produced by several layers of frozen spray which is emitted as a dense water fog from the carriage. Consequently, the ice is grown *upwards* unlike sea ice, where the ice grows into the water. The tank water is sprayed from a height of $\approx$ 1.7 m at an ambient temperature of $\approx$ -12°C onto the water surface. The tank water contains 0.3 % ethanol to weaken the ice in order to achieve the desired scalability of sea ice according to Froude and Cauchy similitude (Jalo-

nen and Ilves, 1990; Riska et al., 1994 and Li and Riska, 2002, see Equation 1.1, 1.2). The scaled and directly adjusted parameters are common thickness and bending strength (according to ITTC, 2002). The strength is adjusted by a low temperature consolidation phase (as low as -15°C) after the spraying. Thereafter, the temperature is increased to between 0°C and -2°C in the tempering phase to re-adjust the strength to the target and to reduce the temperature and ice property gradient within the ice.

Figure 3.2. Ice tank at Aalto University.

3.2.2 Summary of the Mechanical Behavior of Model-Scale Ice in the Context of Sea Ice

As emphasized in Section 1.1, the focus of this thesis is to create a sound basis for the development of a virtual ice tank [2] for ships in ice and to determine how to effectively simulate the mechanical behavior of model-scale ice. The tests presented in PI are aligned with the recommendations of ITTC (2002), which propose a test speed of 1 mm/s for flexural strength tests. It is acknowledged that the proposed loading rate of 1 mm/s for cantilever beams may lead to different strain-rates, depending on the dimensions of the specimen; nevertheless, it is considered as a target value to obtain elastic deformation. However, it is reported that some types of model ice appeared to deform plastically (Schwarz, 1977; Jalonen and Ilves, 1990), visco-elastically (Zufelt and Ettema, 1996) or visco-plastically (Moores et al., 2001).

[2]The concept of the virtual ice tank is explained in the future work (Section 7.2) to which this thesis contributes.

Generally, model-scale ice must be considered as a material that can differ from sea ice in its constitution and its mechanical behavior. Furthermore, the properties of model-scale ice are significantly less explored than those of sea ice and are often based on assumptions related to macroscopic observations. The presumption of analogies between both materials can be considered as valid starting points on a macro-scale, but are yet to be proven.
The scope of this thesis covers experiments in tension, compression and bending. As stated in Section 3.1, sea ice may be considered strain-rate insensitive in tension and bending, while in compression ice can exhibit significant strain-rate sensitivity. Therefore, prior to the work of this thesis, tensile and compressive tests conducted with different loading rates (Figure 3.3) [3]. The variation of loading rate (i.e. strain-rate) shows neither an impact on the nominal stress (Figure 3.3) nor on the stiffness Wegner (2011).

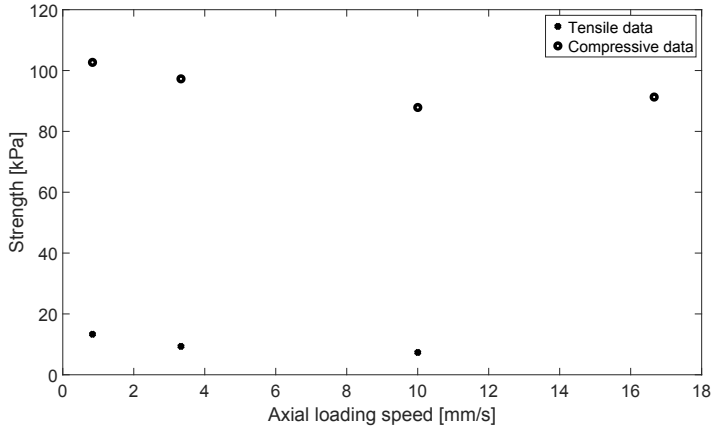

Figure 3.3. Average tensile and compressive strength as a function of loading rate (data from Wegner, 2011).

On the basis of experience in ice tanks, it is assumed that the grains of model-scale ice are of high strength compared to the bonds between them. Therefore, trans-granular cracks are not considered to occur. Furthermore, Timco (1981b) reported that in bending tests with ice from impure melt that the failure frequently occurs along the grain boundaries. This is another difference compared to sea ice or fresh water ice where trans-granular cracks occur; according to Gold (1970), as many as 2/3 of all cracks are trans-granular.

[3]The velocity of ship models in model-scale ice lies often between 0.1 m/s to 1 m/s

4. Experiments with Model-Scale Ice [PI, PIII]

4.1 Grain Size Measurements ([PI])

Grain size measurements are usually conducted using thin sections. However, the Aalto model-scale ice is too weak, every thin-section attempt at the ambient temperature of the ice tank, between 0°C and -2°C, failed because the thin slice of ice could not support itself. Furthermore, the inter-granular cohesion is apparently significantly weaker than the strength of the individual grains so that any attempt at cutting the specimen led to *shaving off* an entire grain layer and ultimately, to the destruction of the specimen. In order to assess the grain-size the grains are carefully separated from the ice pieces with a cold blade. This produces an image as displayed in Figure 4.2 with single grains distributed over the surface between the polarized light filters. This allows solely for an assessment of the grain-size, but not of the overall ice structure, which is however considered sufficient here. The grain-sizes are measured with digital image processing and the results are found following a lognormal distribution (Figure 4.2), with a highest probability density, i.e. mode value, of 0.68 mm. Additional information can be found in PI.

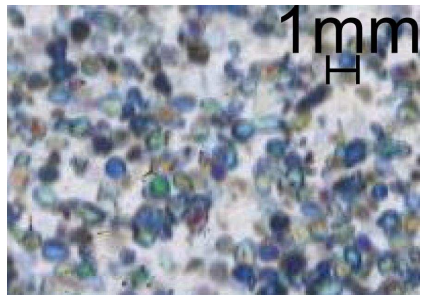

Figure 4.1. Ice grains of Aalto model-scale ice (PI).

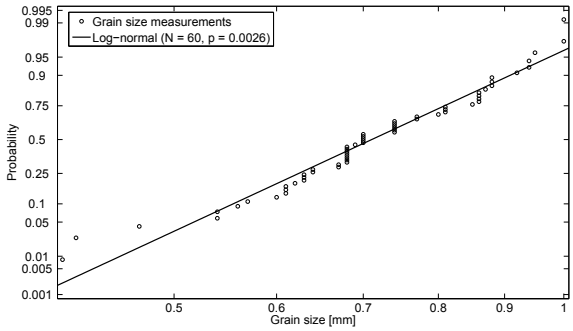

Figure 4.2. Log-normal distribution of measured grain sizes with 60 samples (PI).

4.2 Elastic Modulus [PI, PIII]

The *elastic modulus* here is the linear elastic relationship between the elastic strains and the related stresses. The nature of experimental methods that apply physical strain to the ice to determine the *elastic modulus* are defined in other sources as the *elastic strain modulus* (e.g., Timco and Weeks, 2010) or *strain modulus* (e.g. Tatinclaux, 1988). In this thesis the term *elastic modulus* is used, because the results of the strain experiments to determine the elastic modulus are later implemented in the numerical model as the elastic modulus (PII and PIII).

The macroscopic elastic modulus is determined by loading the intact ice sheet with weight increments, while measuring the ice sheet deflection. The loading and unloading is done repeatedly to assess whether the deformation can be fully recovered after unloading. The deflection that is encountered is in the order of micrometers and is measured with a laser displacement transducer of high resolution. This device is mounted in the center of a tripod with a 2 m span-radius. The weight of the system and its heat exchange with the ice cause the tripod to carve into the ice. This leads to a slight relative movement between the tripod and the ice sheet, which in turn affects the measured displacement. Because of this, the displacement measured over time in Figure 4.3 is slightly curved and not straight.

The macroscopic elastic modulus, which is considered to be constant through-thickness, is defined according to Kirchhoff plate theory in Equation 4.1 (see also ITTC, 2002) with the loading force, F, the ice thickness, h, the displacement measured δ, and the foundation factor, k, which is the product of gravitational acceleration and the density of the water (Equation 4.1).

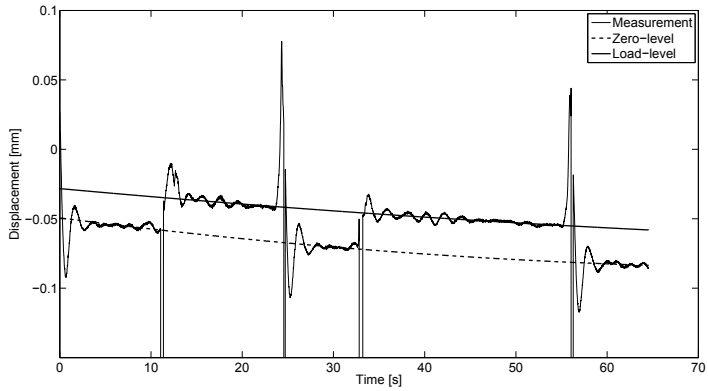

Figure 4.3. Time-history of an ice sheet deflection measurement (PI).

$$E = \frac{3}{16}\frac{1-\nu^2}{kh^3}\left(\frac{F}{\delta}\right)^2 \tag{4.1}$$

The average macroscopic elastic modulus with a constant distribution over thickness [1] of the experiments would be around 108 MPa with a maximum load of 56 g at 0.056 mm displacement (see PI, Equation 4.1 and Figure 4.4). However, the next higher weight increment of 109 g causes a reduction of the strain modulus by 25 % (see Figure 4.4) and is associated with partial plasticity as the deformation cannot be fully recovered (see PI, Figure 4.5). Figure 4.4 indicates the theoretical continuation of elastic response up to the load that causes a partly plastic response (Figure 4.5). Furthermore, the possible range of loads causing plastic deformation is marked in Figure 4.4.

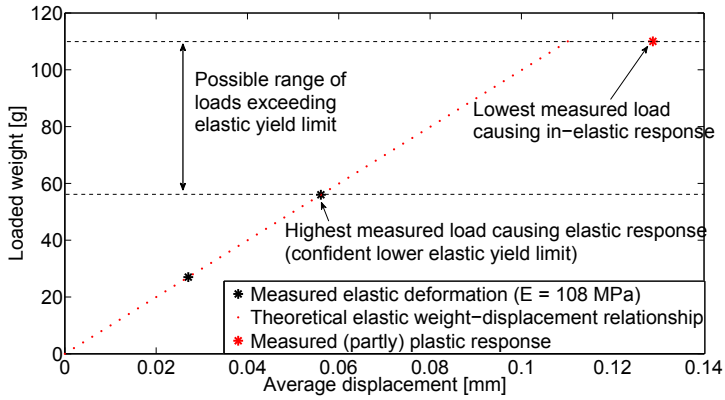

Figure 4.4. Graphical representation of the measured linear elastic range, the measured in-elastic (plastic) response and the possible range of loads causing plasticity.

[1] This is the standard according to ITTC (2002).

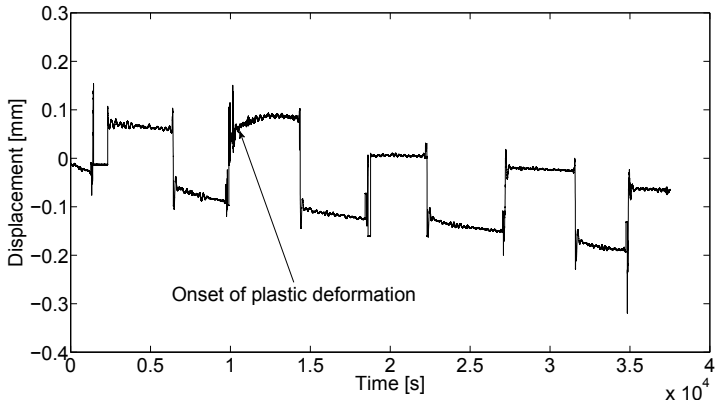

Figure 4.5. Deflection of an ice sheet causing elastic-plastic response (see also PI).

4.3 Tensile, Compressive and Flexural Experiments [PI]

The experiments on the ice properties are conducted for tension, compression and downward bending. In all the experiments the displacement, response force and specimen dimensions are measured. Figure 4.6 shows the specimens for the ice property experiments, i.e. for tension, compression and bending (from left to right) cut from 25 mm thick ice. The tensile specimens have a ring-shaped head at which the loading force of the linear drive acts and pulls the specimen to cause failure at the thinning part between the ring and the adjacent ice sheet. The minimum width is 25 mm, equal to the thickness. The compressive specimen has the shape of a small cube, i.e. 25 mm x 25 mm, with one side attached to the ice sheet. The dimensions of the cantilever beam follow the recommendations of ITTC (2002) with a width of 58 mm and a length of 175 mm to 170 mm, a loading point about 15 mm from the tip and a thickness of 25 mm. All specimens are tested at the same speed of 6 mm/s (PI).

The setup of the measurement units and the loading device is displayed in Figure 4.7. In all the experiments, the same devices are employed. All specimens are tested at the same speed of 6 mm/s (PI).

The compressive specimens are loaded horizontally and their failure starts from random locations at the plain impact face (Figure 4.9, PI). The tensile specimens are loaded at the ring and fail at or near the thinnest cross-section, as in Figure 4.8. The bending specimens are loaded vertically downwards and fail at the transition between beam and ice plate.

The force-displacement measurements obtained for compression, tension and

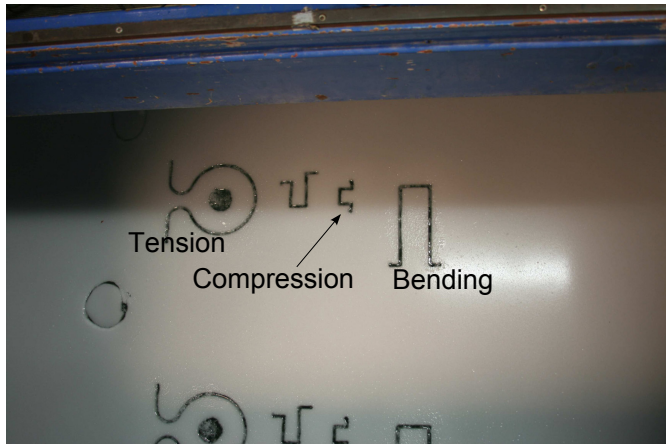

Figure 4.6. Model-scale ice property experiments.

bending are found in PI, PII and PIII and are replotted in Figure 4.10, 4.11 and 4.12. In all measurements the maximum force is used as the representative value for the sustainable force. In all cases, the maximum force refers to the global peak in the loading history, which is at the same time the point of the specimen failure. The experimental data are compiled in Appendix A.

4.4 Measurement Accuracy

The measurement accuracy of the bending strength, which is calculated from the force and dimensional parameters, is treated in PIII. The accuracy of the entire bending strength is a function of its components and inherent accuracies for which the available standard of ITTC (2005) is used here. The total accuracy is mainly affected by the dimension measurements as an indentation of 1 mm to 1.5 mm at the softer bottom layer may easily occur [2]. Figure 4.13 shows a broken tensile test-specimen with the hard top-layer, the soft bottom layer and the gradual transition in texture in between. Consequently, in PIII the total accuracy is calculated for the bending strength of 59.1 kPa is ±8%.

[2]Other measurements refer to an accuracy above 99.9% (see PIII).

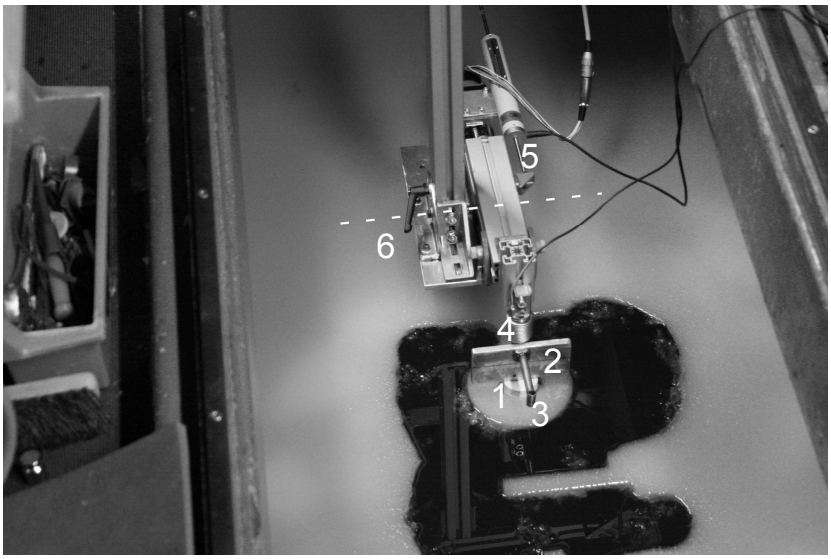

Figure 4.7. Device for model-ice specimen tests, with: 1) a round cylinder for loading tensile rings, 2) a plate for compressive tests, 3) a plunger for flexural tests with the cantilever beam, 4) the load-cell, which records force signals in all three load cases, 5) a displacement transducer, which records displacements in all load cases and 6) the loading fame, with indicated rotation axis (PI).

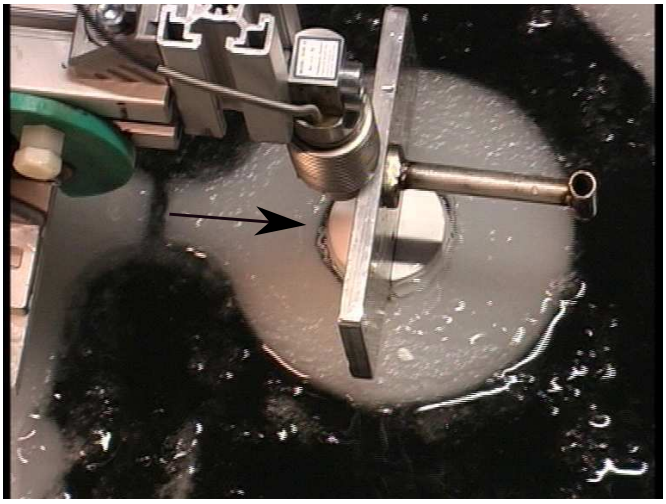

Figure 4.8. Tensile specimen after failure.

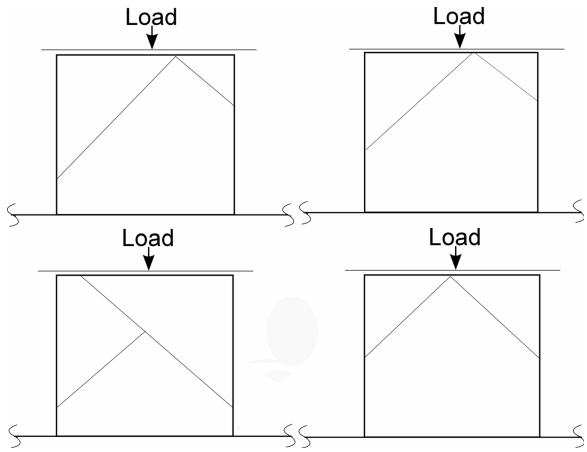

Figure 4.9. Failure patterns of compressive specimens observed in experiments (PI).

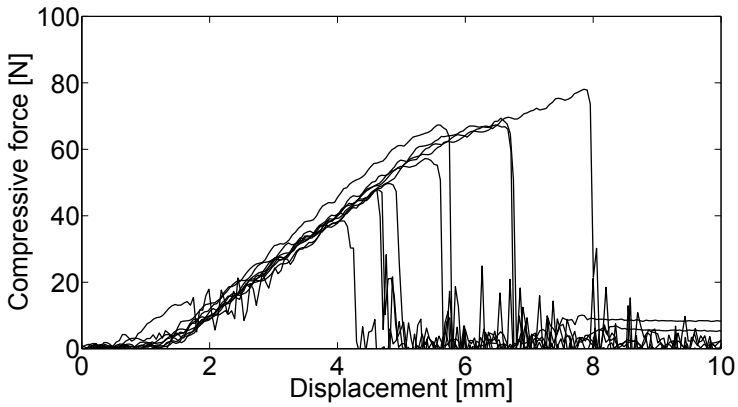

Figure 4.10. Compressive specimen measurements (see also PI) and PII).

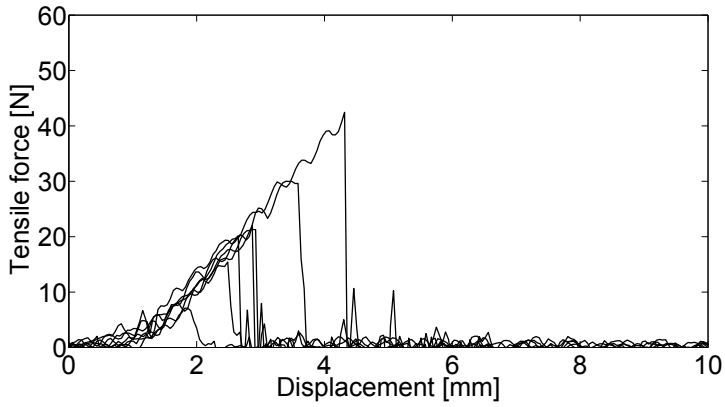

Figure 4.11. Tensile specimen measurements (see also PI and PII).

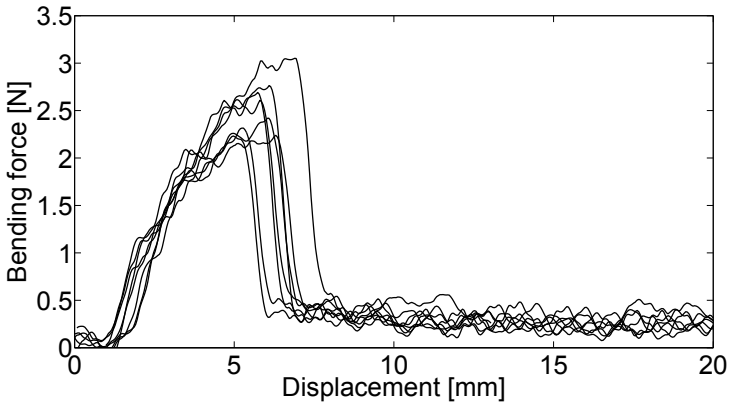

Figure 4.12. Cantilever beam bending measurements (see also PIII).

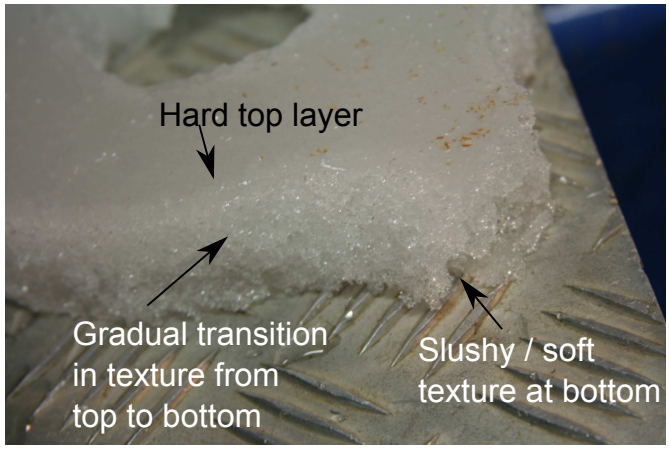

Figure 4.13. Tensile specimen extracted from the tank after testing.

5. A Numerical Model for Model-Scale Ice [PI, PII, PIII]

5.1 The Background of the Numerical Model [PII]

The purpose is to build a numerical model on micro-scale that reflects the mechanical behavior on macro-scale, while including experimental findings. The element size is aligned with the predominant grain-size of the model-scale ice [1], which is considered to be the *reference element size*. Operational experience in the ice tank shows that a significant amount of water is trapped within the model-scale ice. In this context Li and Riska (2002) defined a strength index for the Aalto model-scale ice on the basis of the contained amount of unfrozen liquid, which weakens the material. Consequently, the voids, i.e. inclusions of water and air, are incorporated into the model. Their size is assumed equivalent to the grain size (see Figure 5.1). Figure 5.1 shows the composition of the numerical model with the air elements removed, one example marked (1), and water elements colored brown marked (2).

The material model (153_Damage3 in LS-DYNA) relates to the work of Lemaitre and Desmorat (1992) as it includes damage softening. Figure 5.2 shows a compressive measurement (see also Figure 4.10), where softening is observed, which is considered to be associated with damage.

The damage is considered to represent physically the increasing number of micro-cracks in the grain boundaries, which are considered to lose coherence with increasing strain. According to Chaboche (1987), all processes prior to macro-crack initiation, such as micro-crack initiation and micro-crack propagation, are considered part of the damage mechanics, whereas fracture me-

[1] The grain-size is in general considered an invariable parameter in the ice production process as all parameters (droplet size, water pressure in pipes, ambient and water temperature) are invariable.

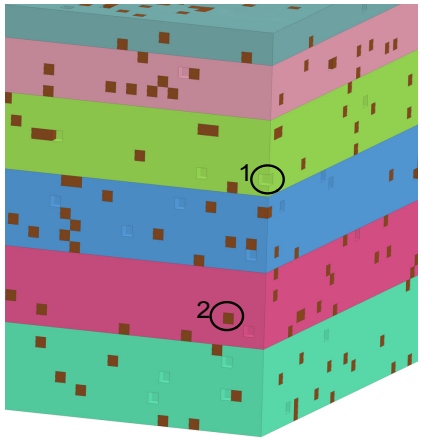

Figure 5.1. Composition of the numerical model-scale ice model, with air voids marked (1) and water elements marked (2).

chanics begin at the point of macro-crack initiation. As the failure observed in the experiments grows quickly and occurs almost instantly, fracture mechanics are not considered for the tests presented in this thesis. The voids of air and water are explicitly modeled by removing the elements representing air pockets, while the water elements are modeled as elastic fluid (LS-DYNA material model 001 _Fluid_Elastic_Fluid). The amount of voids is determined based on the model-ice density (911 kg/m^3)[2], which results in 5.5% porosity (1% air and 4.5% water). The voids are distributed randomly over the entire specimen.

Compared to sea ice or fresh water ice, model-scale ice and especially fine-grained model-scale ice is a sparsely researched material. Consequently, on the basis of the state of the art, the numerical model is aligned to two modeling approaches. One is aligned with ITTC (2002), assuming constant material properties through-thickness, and the second one is an exponential distribution of properties through-thickness for the bending of cantilever beams on the basis of Kerr and Palmer (1972). The through-thickness distribution of the elastic modulus in sea ice is significant for the bending behavior, which is found in generalized form in Reddy (2011) for functionally graded beams. The theory of a stronger top and weaker bottom of the model-scale ice is supported by operational ice tank experience and observations made by Timco (1981a); Valkonen et al. (2007).

[2]Pure ice is assumed to be 917 kg/m^3 and tank water is measured as 989 kg/m^3 (see PI).

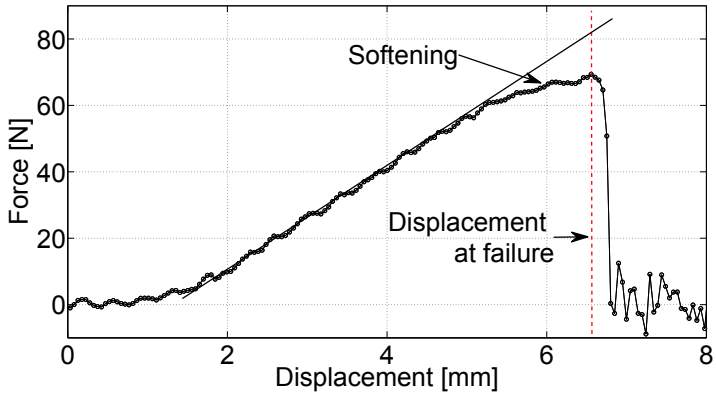

Figure 5.2. Force-displacement curve of a compressive experiment and simulation with indicated simulation progression without damage. The section in which *softening* manifests is considered to refer to a significant accumulation of micro-cracks. Once those reach a critical threshold a macroscopic crack forms leading to the failure of the specimen.

5.2 The Numerical Model of Model-Scale Ice [PI, PII]

5.2.1 A Functionally Graded Property Model for Cantilever Beam Tests

The strength properties of the model-scale ice appear to change over thickness. In bending, the response of a cantilever beam depends on the actual distribution of the strength properties as the bending stiffness of a layer depends on the second moment of inertia and the strain modulus, S [3]. The second moment of inertia, I, of a rectangular cross-section, A, with width, b, and height, h, additionally depends on its vertical distance to the neutral axis, za (see Equation 5.1 and Figure 5.3). The subscript, L, indicates here a layer inherent property.

$$SI_{total} = \sum_{i=1}^{n} S_{L,i} \frac{b \cdot h_{L,i}^3}{12} + b \cdot h_{L,i} \cdot za_{L,i}^2 \tag{5.1}$$

The distribution of properties through-thickness, *f(z)*, for the model-scale ice in this thesis is defined by the exponential Equation 5.2 with the thickness coordinate z and the coefficients a and b with the set exponent - *0.5*. An exponential function is selected. Kerr and Palmer (1972) used an exponential function [4] for the elastic modulus variation through thickness in sea ice. Furthermore, as the top of the model-scale ice is apparently of higher

[3] This may be an elastic modulus or a plastic strain modulus.
[4] This is analogous to Reddy (2011) for functionally graded beams.

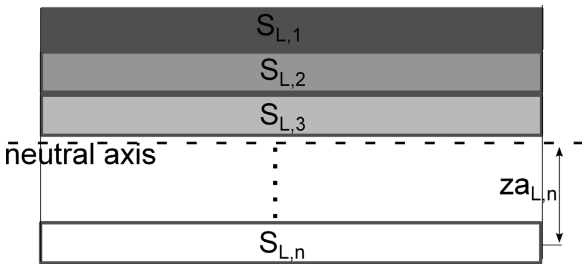

Figure 5.3. Schematic variation of stiffness properties through-thickness with reference to Equation 5.1.

strength compared to lower layers (see, e.g., Valkonen et al., 2007), the distribution requires a significant gradient, for which an exponential function is well suited.

$$f(z) = a + b \cdot z^{-0.5} \tag{5.2}$$

The coefficients a and b are defined by boundary conditions, which are defined in agreement with the experiments, such as, e.g. the total axial stiffness in tensile tests (see PIII).

5.2.2 A Model with Constant Properties Through Thickness for Uni-Axial Tests

On the basis of available information and the nature of the load case, appropriate simplifications are made. The guidelines of ITTC (2002, 2014) consider the model-scale ice as homogeneous and isotropic material. Unlike in bending, the response in tension and compression is a simplification considered independent from the actual distribution of strength properties through thickness [5]. Consequently, the summation over the number, (i = [1;n]), of individual layer stiffnesses, S_L, times the layer cross-section, A_L, equals the average stiffness, S_{avg}, times the total area, A, (see Equation 5.3).

$$\sum_{i=1}^{n} S_{L,i} A_{L,i} = S_{avg} A \tag{5.3}$$

The available measured parameters are the total axial force, F_x, and the axial displacement, u_x, in coordinate direction x. The force, F_x is represented in Equation 5.4 as a function of the axial strain. Both sides of Equation 5.3 can be interchanged with each other in Equation 5.4.

$$F_x = S_{avg} A_L \frac{\partial u}{\partial x} \tag{5.4}$$

[5] This means the distribution does not affect the response force. However, Reddy (2011) showed that this is not exactly valid.

5.2.3 The Material Models in LS-DYNA

The material models that are introduced in this section are applied on solids with eight nodes.

The Damage Model for Ice Elements

The applied material model in LS-DYNA is 153_Damage3. This particular material behavior is linear elastic until the yield stress. Thereafter the plastic regime starts, in which the stress-strain relationship is governed by the hardening modulus, while *damage* causes additional softening of the material. Failure occurs once the critical damage is reached (see Figure 5.30).

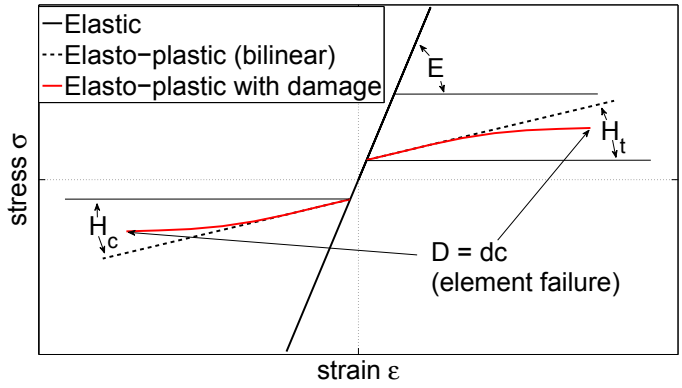

Figure 5.4. A principle illustration of stress-strain behavior of the damage material in comparison with an elastic and an elasto-plastic (bilinear) material. It must be noted that the exact definition and shape varies in compression and tension as well as through-thickness in bending. The subscripts t and c denote tension and compression.

The damage evolution, $\dot{D}$, is defined by the strain energy release rate, Y, the damage resistance parameter, S, the exponent, t_d, and the equivalent plastic strain-rate, $\dot{\epsilon_p}$, (Equation 5.5). The damage value, D, evolves from 0 to (just less than) 1. The material fails once the damage, D, is equal to the predefined critical damage value, dc, which is maximum tolerable damage.

$$\dot{D} = \begin{cases} \left(\frac{Y}{S}\right)^{t_d} \dot{\epsilon_p} & ,r > r_d \;\&\; \frac{\sigma_H}{3\sigma_{vM}} > -\frac{1}{3} \\ 0 & ,\text{otherwise} \end{cases} \tag{5.5}$$

The damage evolution in Equation 5.5 is coupled on the stress tri-axiality, $\frac{\sigma_H}{3\sigma_{vM}}$, [6] and the damage threshold, r_d. The damage threshold is the accumulated plastic strain at which the damage starts to accumulate. In this thesis

[6] σ_H is the hydrostatic stress and σ_{vM} the von Mises stress.

the damage threshold is equal to zero in order to accumulate damage directly after yielding (r_d is equivalent to EPSD in Table B.0.1).

The accumulation of the damaged plastic strain, r, which is used in this thesis, follows Equation 5.6 as a function of the damage, D, and the equivalent plastic strain-rate, $\dot{\bar{\epsilon}}_p$, (Equation 5.7).

$$r = \int (1 - D)\dot{\bar{\epsilon}}_p \tag{5.6}$$

The plastic strain-rate is defined according to Equation 5.7 as a function of the associated plastic flow, $\dot{\epsilon_p}$, as defined in Equation 5.8. The plastic flow is a function of the equivalent von Mises stress σ_{vM}, the stress deviator, s^D, and a plastic consistency parameter $d\lambda$ (for additional information, see LS-DYNA (2013)).

$$\dot{\bar{\epsilon}}_p = \sqrt{\frac{2}{3}\dot{\epsilon_p}\,\dot{\epsilon_p}} \tag{5.7}$$

$$\dot{\epsilon_p} = \frac{3s^D}{2\sigma_{vM}} d\lambda \tag{5.8}$$

The energy release rate, Y, in Equation 5.5 is defined by the elastic strain, ϵ^{el}, and the elasticity tensor, T^{el}, following Equation 5.9 (LS-DYNA, 2013).

$$Y = \frac{1}{2}\epsilon^{el}\, T^{el}\, \epsilon^{el} \tag{5.9}$$

The stress after yielding, σ, is defined by the isotropic hardening modulus (equivalent to the tangent modulus), H, the plastic strain, ϵ_p, and the yield strength, σ_y, in Equation 5.10.

$$\sigma = \sigma_y + H\epsilon_p \tag{5.10}$$

The stresses, σ_d, are the undamaged stresses, σ, modified by the damage, D, defined in Equation 5.11.

$$\sigma_d = \sigma(1 - D) \tag{5.11}$$

The Fluid Model for Water Elements

The water elements are represented by the material model of an elastic fluid (001 _Fluid_Elastic_Fluid, see LS-DYNA, 2013). The resulting pressure rate, $\dot{p}$, is defined by the bulk modulus, K, and the volumetric strain-rate, $\dot{\epsilon_{jj}}$, in Equation 5.12.

$$\dot{p} = -K\dot{\epsilon_{jj}} \tag{5.12}$$

The deviatoric stresses, σ_{ij}, are defined by tensor viscosity coefficient, VC, a characteristic element length, ΔL, the fluid bulk sound speed, a, the fluid

density, ρ_w, and the deviatoric strain-rate, $\dot{\epsilon_{ij}}$ in Equation 5.13.

$$\sigma_{ij} = VC \cdot \Delta L \cdot a \cdot \rho_w \dot{\epsilon_{ij}} \tag{5.13}$$

In case of a fluid, the input parameters are the fluid density, $\rho_w = 989$ kg/m^3, the bulk modulus of water, $K = 2.15 \cdot 10^9$ Pa, the tensor viscosity coefficient is set to a default value, $VC = 0.1$, as well as the cavitation pressure, $CP = 1 \cdot 10^{20}$ Pa.

5.3 Definition of Material Parameters

This section describes the method that is used to define the material parameters for a model where properties are a constant through-thickness (PII) which can be applied for uni-axial tests and a functionally graded model for cantilever beam bending. The property values for the material model 153_Damage3 described in Section 5.2.3 are stated in Table 5.1 and the following subsections provide more information on the particular parameters.

Table 5.1. Summary of material properties for the functionally graded material (PIII) and the material with constant properties through-thickness (PII). The material constants, i.e. the damage resistance $S = 25$ Pa and exponent $t_d = 2$ are the same in both models (PII, PIII).

Thickness / z-coordinate [mm]	Elastic modulus, E [MPa]	Yield strength, σ_y [kPa]		Hardening modulus, H [MPa]		dc	
		Tens.	Comp.	Tens.	Comp.	Tens.	Comp.
Material properties functionally graded over thickness							
0 to 2	770	7.5	23	21.5	0.84	0.0017	0.0065
2 to 5	197	4.5		5.2			0.025
5 to 10	118	2.5		3.0			0.085
10 to 15	78	1.8		1.8			0.13
15 to 20	56	1.4		1.16			0.4
20 to 25	43	1.2		0.76			0.55
Material properties constant through-thickness for uni-axial specimen tests							
0 to 25	148	0.45	0.45	3.07 [a]	1.14 [b]	0.001 [c]	0.036 [d]

[a] average, full range: 2.8 - 3.3
[b] average, full range: 0.95 - 1.3
[c] log-normal median, full range: 5.0 $\times 10^{-6}$ - 3.4 $\times 10^{-2}$
[d] log-normal median, full range: 0.005 - 0.236

5.3.1 Elastic Modulus

The Elastic Modulus Constant Through Thickness

The elastic modulus is determined by experiments (see Section 4.2), from which load and displacement are recorded. A linear elastic model of finite elements is built which is loaded with the same load as in the experiments. The elastic modulus is iteratively modified to obtain the measured displacement of 0.056 mm at the same load as in the experiments (56 g, see also Figure 4.4). In the isotropic case the mesh size is 25 mm for which an elastic modulus of 148 MPa is determined (PII).

On the basis of increased computational resources in PIII a mesh size sensitivity study is conducted (Figure 5.5) [7], for which an average elastic modulus of 110 MPa is determined, which is in agreement with the analytical solution (Equation 4.1) of 108 MPa.

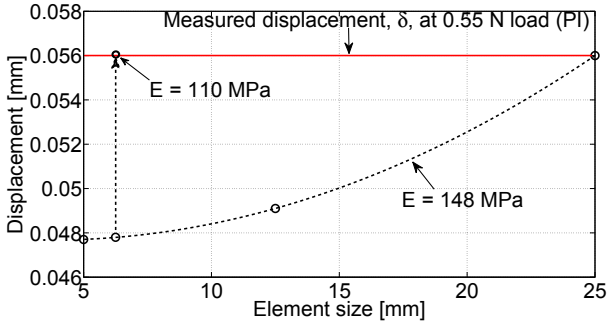

Figure 5.5. Mesh size dependency of displacement results in reproducing the deflection of an infinite plate on elastic foundation. The figure is an extension of what is found in PIII.

The Functionally Graded Elastic Modulus

In the functionally graded model the distribution of the elastic modulus follows Equation 5.2. The boundary conditions to define the unknown coefficients of Equation 5.2 are the average elastic modulus of 110 MPa and the value of the top layer. The elastic modulus in the top layer, E_{top}, is taken as seven times the average elastic modulus (see Equation 5.14). The factor seven refers to an assumed analogy to the distribution of the tensile hardening modulus for which a line of arguments defined this relationship (see PIII).

$$\frac{E_{top}}{E_{av}} = \frac{H_{t,top}}{H_{t,av}} = 7 \tag{5.14}$$

[7] The figure shows the smallest computationally feasible discretization.

The factor seven refers to an assumed analogy of the distribution of the tensile hardening modulus (see Section 5.3.3). The top layer being seven times the average stiffness provides a good compliance of numerical results and experimental data in uni-axial tension and cantilever beam tests (see PIII). Figure 5.6 represents the distribution of the elastic modulus, which is considered being invariant for compression and tension, i.e. loading direction independent.

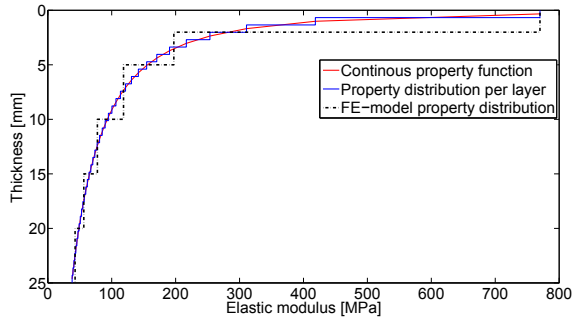

Figure 5.6. Distribution of the elastic modulus (PIII).

5.3.2 Yield Strength

The Yield Strength Constant Through Thickness

The yield strength of the model with constant properties through thickness is the same for both tension and compression. The yield strength is considered to be the lowest confident yield limit, i.e. the highest elastic stress von Mises stress at 56 g load (see Figure 4.4). The yield strength, $\sigma_y = 0.45$ kPa [8], is determined with the same model used in Section 5.3.1. As Figure 4.4 indicates the actual yield strength might be higher, but still be of the same order of magnitude as $\sigma_y = 0.45$ kPa, consequently, a minor variation of its absolute value would not affect the simulated failure processes.

The Yield Strength of the Functionally Graded Model

The tensile yield strength at the bottom of the functionally graded model-scale ice is determined in analogy to the yield strength, which is constant through-thickness. It is considered that Figure 4.5 shows partly plastic deformation and remaining elasticity. Consequently, it is assumed that only bottom layers yield in the experiments which are strained in tension, as shown in Figure 5.7.

The tensile yield strength is distributed over thickness by Equation 5.2 and

[8] This value is used in all simulations with constant properties through-thickness.

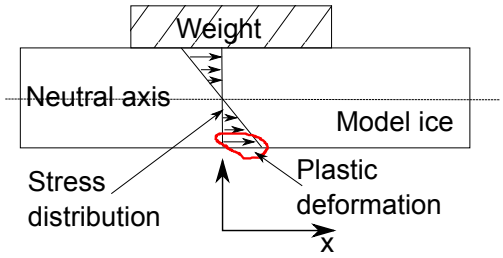

Figure 5.7. Principle stress distribution in a loaded infinite plate as in Figure 4.5. Compressive stresses act above the neutral axis and tensile stresses below. The material exceeds the elastic yield limit in the bottom layer which is marked in red. This effect is considered to cause the plastic deformation encountered in Figure 4.5.

the second boundary value, the tensile yield strength on top (7.5 kPa), is determined iteratively as the highest possible value that maintains compliance with the experiments (see Figure 5.8 and Table 5.1). With reference to Figure

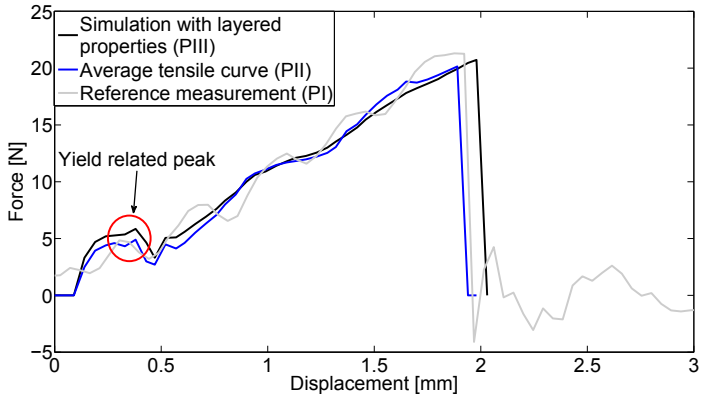

Figure 5.8. Tensile simulations with highlighted yield related peak (PIII) together with a reference measurement of a similar maximum force.

5.7, the experiments neither provide direct evidence for the value of the compressive yield strength nor for its distribution. In order to simplify the model the compressive yield strength of the functionally graded model is taken as a constant value through thickness of 23 kPa (Table 5.1). The compressive yield strength remains the only unknown and is treated as free parameter which is defined to achieve compliance of the cantilever beam simulation with the experiments. However, the compressive yield strength of 23 kPa causes an offset in the displacement (see Figure 5.9) [9].

[9] See also PIII and the Discussion in Section 7.2 for additional information.

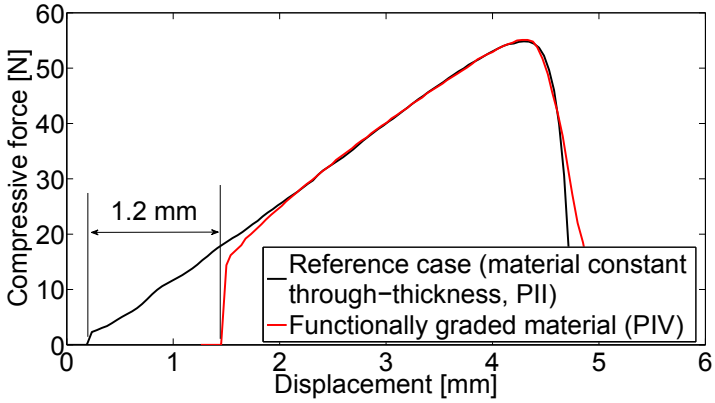

Figure 5.9. Compressive force displacement curves of the functionally graded model together with the reference model with properties constant through thickness.

5.3.3 The Hardening Modulus

The Hardening Modulus as Constant Through-Thickness

The hardening modulus governs the stress-strain relationship in the plastic regime (Figure 5.30). The tensile and compressive hardening modulus is determined for all uni-axial experiments (see Figure 4.10 and 4.11). The tensile and compressive average values are used as representative values to calibrate the functionally graded model (Table 5.1).

Examples of simulated force-displacement curves plotted against their reference measurements are found in Figure 5.10 for compression and 5.11 for tension. Force-displacement plots with stress distribution at different displacement instances are found in Appendix C.2 for tension and in Appendix C.3 for compression.

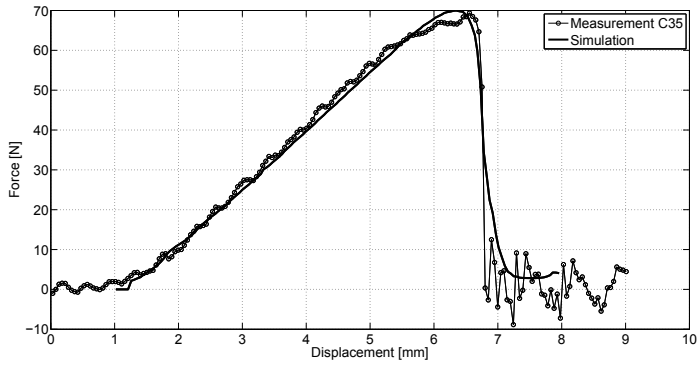

Figure 5.10. Compressive simulation with associated measurement (PII).

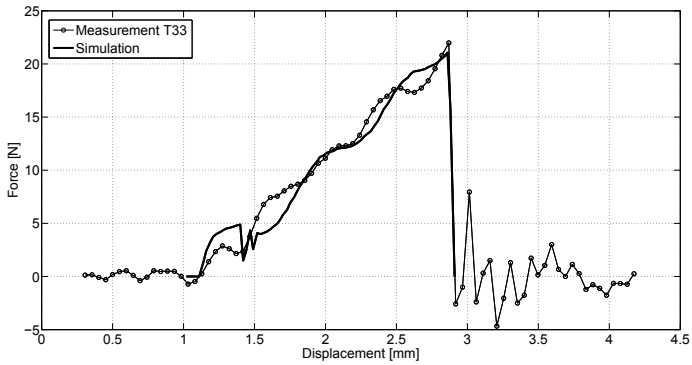

Figure 5.11. Tensile simulation with associated measurement (PII).

In order to simulated the global stiffness of the cantilever beam a hardening modulus of 20 MPa is required which is constant through-thickness. This value is seven times greater than the tensile hardening modulus (Table 5.1) and indicates possible conflicts when representing tensile and flexural behavior in a model which properties are constant through-thickness.

The Hardening Modulus of the Functionally Graded Model

Cantilever beam simulations with constant properties through thickness require a hardening modulus of around 20 MPa in consequence of which the tensile hardening modulus on top of the functionally graded material is considered to be seven times greater than the average tensile hardening modulus (Table 5.1).

In order to determine the coefficients of Equation 5.2 two boundary values are required. For the hardening modulus, one boundary value is the hardening modulus of the top layer (see also Equation 5.14) and the other is the global plastic stiffness (thickness x isotropic hardening modulus). However, this delivered too weak of a response, in consequence of which the thickness of the strong top layer is increased by two layers to around 2 mm, which coincides with the freeboard of the ice sheets (see the black dashed line in Figure 5.12).

Figure 5.13 shows the stress distribution of the functionally graded model, where the stresses in the top-layer are significantly higher than in lower layer.

A hardening modulus, which is constant through-thickness, is also used for the cantilever beam model to assess its order of magnitude. Its value is approximately seven times greater than the average tensile hardening modulus. This value is used as tensile hardening modulus of the top-layer for the functionally graded material (see also Equation 5.14). The exponential distribution of the

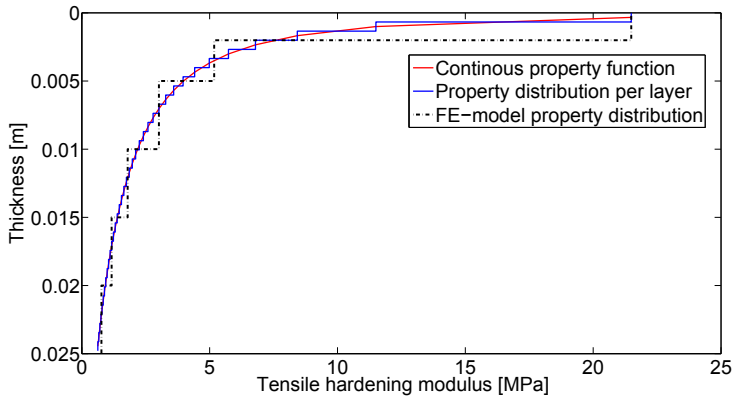

Figure 5.12. Distribution of the tensile hardening modulus through thickness (PIII).

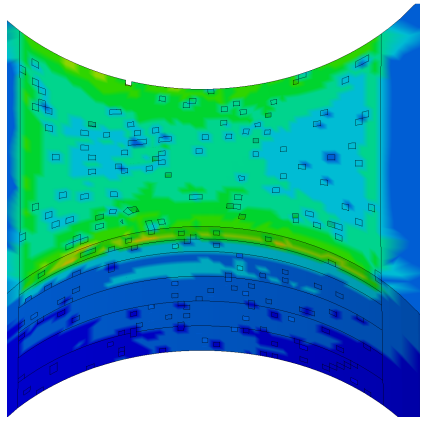

Figure 5.13. Distribution of von Mises stresses in a tensile specimen in the loading process ($\sigma_{vM,max} = 1.4 \cdot 10^5$ Pa) through thickness. Note: Only the center part, where failure occurs, is modeled with layers, the rest has average properties.

tensile hardening modulus (see Figure 5.12 and Equation 5.2) has a nearly vertical course in the lower layers, which take compressive stresses in bending. Numerical experiments with varying ratios of top-layer strength to average strength show a change in the failure pattern for ratios above five, where failure is initiated by the stress-concentrations at the corners between ice sheet and specimen (Figure 5.14), which is not observed in experiments (Figure 4.9). Consequently, the distribution of the compressive hardening modulus is considered less pronounced than for the tensile hardening modulus and is simplified as being constant for the functionally graded model.

5.3.4 The Critical Damage Value

The critical damage value, dc, denotes the point of failure. This value is determined analogously to the hardening modulus iteratively for all uni-axial

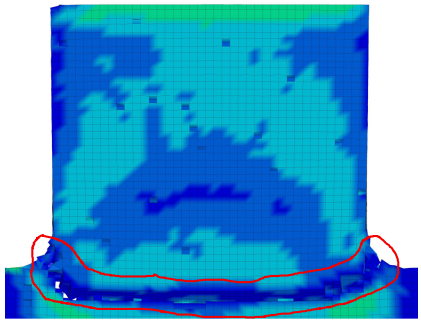

Figure 5.14. Failure pattern in a simulated compressive specimen at a $H_{top}/H_{average}$ ≈5 originating from stress-concentrations in the specimen corners (PIII).

tests (e.g. Figures 4.10 and 4.11) with models that have constant properties through thickness. Furthermore, the dc values are statistically analyzed to define a representative value for tension (Figure 5.15) and compression [10], which is found in Table 5.1. This value is used to define a representative reference force-displacement curve for tension and compression, with which the functionally graded model is calibrated to determine its representative dc values.

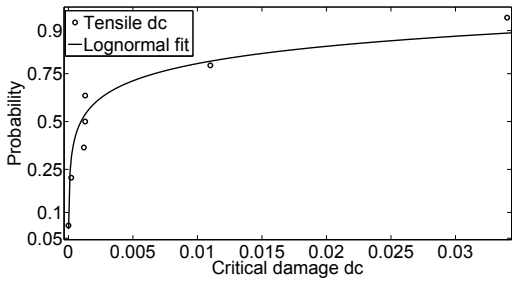

Figure 5.15. Log-normal probability plot of tensile *dc* values.

The value of the tensile *dc* values of the functionally graded model is constant through thickness (see Table 5.1) which is essentially the *dc* value of the top-layer. As shown in Figure 5.13, the strong top-layer dominates the deformation behavior of the numerical specimen and after its failure the entire specimen fails, consequently, the *dc* values of the lower layers cannot be determined.

The failure pattern on top of the functionally graded numerical specimen under compressive load (Figure 5.16a) is in agreement with the experimental observation (Figure 4.9). Over the thickness the failure varies in length di-

[10]The distribution for compression is found in PII.

rection (yellow marking in Figure 5.16b). This is most likely related to the difficulty of determining the *dc* value accurately for each layer [11]. Furthermore, no observations are made that allow an assessment whether this failure through thickness complies with experiments or not.

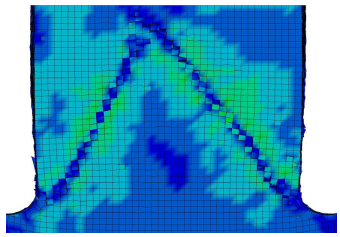

a Failure pattern on top.

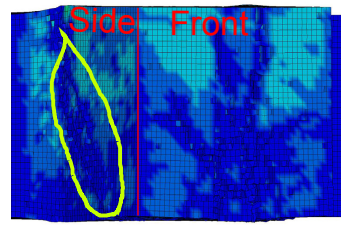

b Angeled view on failed simulated compressive specimen, with marked failure pattern on the side.

Figure 5.16. Failure pattern of the functionally graded numerical specimen in compression.

The "non-synchronous" failure of the numerical specimen through thickness also manifests in the stress-strain relationship of elements through thickness. The failed element in Figure 5.17 is one of the last elements to fail before the specimen failure occurs. The drop in stress in the other elements indicates that surrounding elements fail at this point and that causes missing support for the displayed elements. Furthermore, when the stress in the elements drop the stress in the "failed element" increases. The progression of the stress-strain relationship is also reflected in the force-displacement curve in Figure 5.9.

5.3.5 The Parameter Fitting Technique

The hardening moduli and the dc values for compression and tension in PII are determined iteratively for all uni-axial experiments.The hardening modulus can be determined within an estimated accuracy of at least 5%. This is indicated by the simulations shown in Figure 5.18, where the hardening modulus of 1.25 MPa deviates by 4%, but its deviation from the experimental target can be well identified. The critical damage parameter, *dc*, depends on the damage evolution and is also determined in compliance with the experiments with an accuracy of about 5%, whereas Figure 5.18 shows an example for values differing by 8%. As the *dc* value refers to the point of failure it is considered to be determined uniquely.

[11] See Figure 5.30 for stress-strain curves.

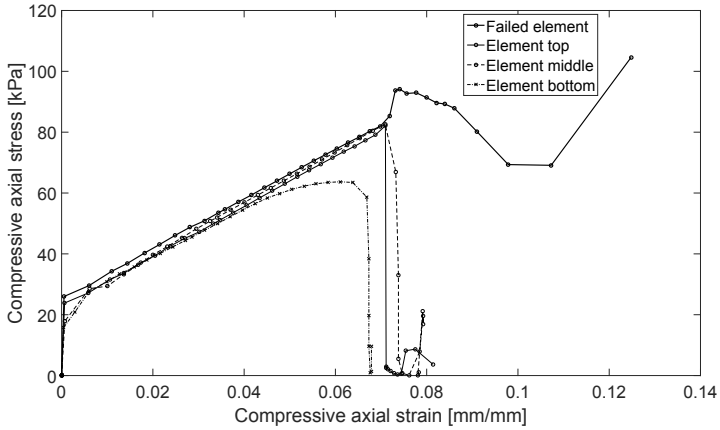

Figure 5.17. Stress-strain relationship in a functionally graded numerical specimen under compressive load. The failed element is within the failure pattern that refers to the ultimate specimen failure. The other three elements are from the impact interface, but do not fail.

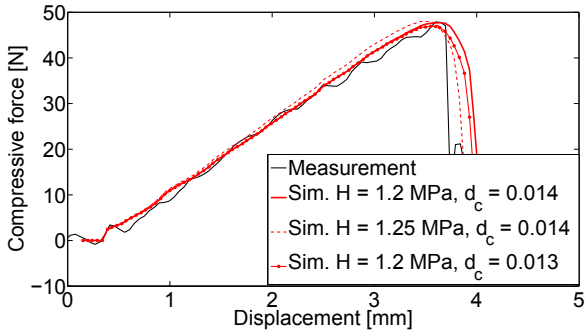

Figure 5.18. A compressive measurement together with simulations of different H and dc values.

5.3.6 Other Constants of the Damage Material

The value of the critical damage value, dc, depends on the damage evolution and therefore on the damage resistance, $S = 25$ Pa, and the exponent, $t_d = 2$ (see Equation 5.5). The damage resistance is systematically increased and $S = 25$ Pa is found to be suitable and applicable for all models in this thesis (see Table 5.1). Figure 5.19 shows the difference between two different damage resistance values.

The exponent t_d is equal to 1 by default, but as Figure 5.19 shows (especially for the blue curves) an exponent of 2 refers to a more rapid failure, which is considered to be in better agreement with the experiments.

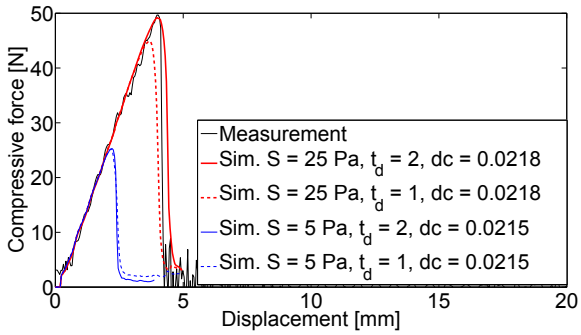

Figure 5.19. A compressive measurement together with simulations of different S and t_d values. The simulations show the accelerated progression of damage with reduced damage resistance and the impact of t_d. In all simulations the material properties are constant through thickness.

5.3.7 The Impact of the Void Density and Distribution

The voids [12] act like local stress concentrators and, consequently, they influence the failure pattern and the location of its initiation. This complies well with experimentally observed failure patterns (see Figure 5.20). A certain variability of the failure pattern is also found for tension in both experiments and simulations (see PII and Figure 3.1e).

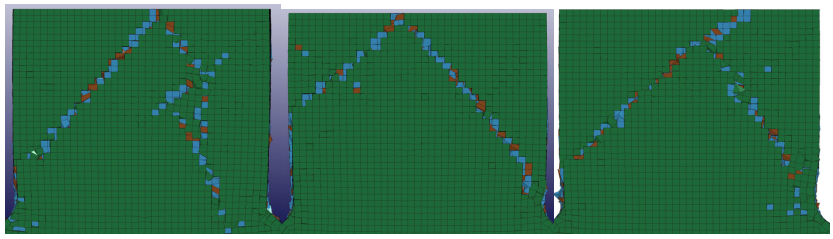

Figure 5.20. Failure patterns of three numerical compressive specimens (PII, top-layer in green to raise visibility of macro-failure).

A comparison of the response forces (see PII, Figure 5.21a) showed that different random void arrangements have a bigger impact on tensile specimens than on compressive ones. However, as the number of possible random variations of the voids is high the sensitivity study in PII is not considered exhaustive. Furthermore, Figure 5.21b shows the sensitivity of simulated compressive specimens on different void densities.

[12] The number of voids is constant, but their location varies randomly.

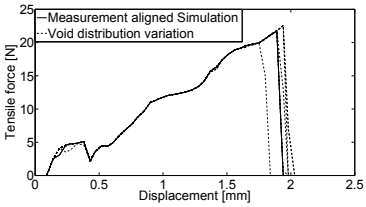

a Sensitivity of a tensile force-displacement results on different random void arrangements of equal density and material parameters

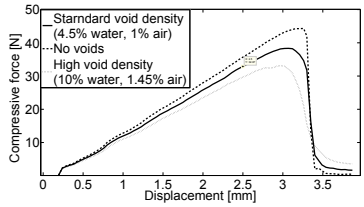

b Sensitivity of compressive force-displacement results on void density variation

Figure 5.21. Sensitivity of simulation results on void distribution and void density (see also PII).

5.4 Strains and Strain-Rate Sensitivity

The modeling of strain-rate effects is not considered in this thesis as the loading time (around 1 second) is considered too short to activate such effects. Therefore, the presented strain-rates are relative rates of strain. In this section the occurring strain-rates in the models for tension, compression and bending is presented with an analysis concluding that strain-rate related effects are not likely to occur. The strain-rates and a discussion on their possible impact is found in the Discussion, Section 7.2. Figure 5.22 shows a numerical tensile specimen with the elements A, B and C, which are selected for the plots of the strain-rates in Figure 5.23. The average strain-rate in the loading process is around 0.05 s^{-1} (see Figure 5.23a) and 0.03 s^{-1} near the root, without considering peaks of local (neighboring elements) or global failure. The strain-rates in Figure 5.23 show a steady and continuous behavior over the course of the loading process, at the end of which, when the numerical specimen fails, a sudden increase in rate is found. This occurs directly after failure in the stress relaxation process. The magnitude of the strain-rate peak at failure is larger closer to the failure interface (Element C) and declines towards the root (Element A).

The global failure occurs right before the peak (Element C, Figure 5.23a). The elements near the thinnest cross-section take the highest stresses (Figure 5.23b). After the global failure the elements relax again, which proceeds at higher rates, when elements are closer to the thinnest cross-section, the location of failure.

Figure 5.24 shows the elements A, B and C to which the plots in Figure 5.25 refer to. As in tension, the strain-rate depends on the analyzed location in the numerical specimen. With reference to Figure 5.25a the representative

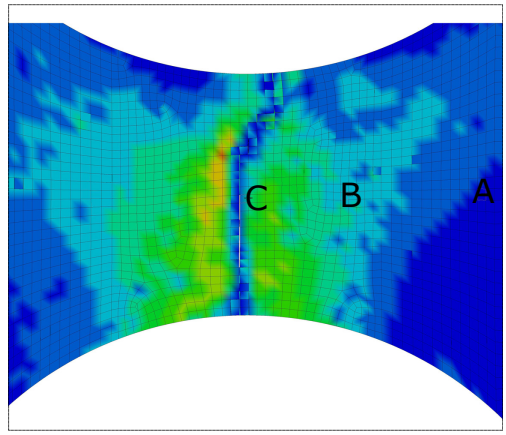

Figure 5.22. A tensile numerical specimen and selected elements for strain-rate analysis.

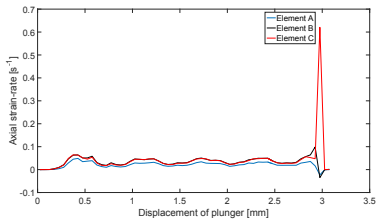

a Tensile strain-rate over plunger displacement for three different elements.

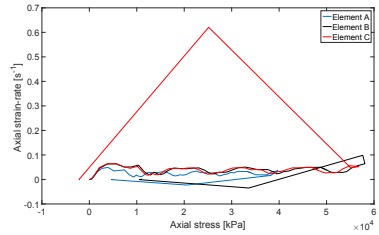

b Tensile strain-rate over stress for three different elements.

Figure 5.23. Strain-rate in a numerical tensile specimen with reference to element locations shown in Figure 5.22.

strain-rate is around -0.1 s^{-1} and -0.05 s^{-1} near the specimen root. As soon as first elements fail within the specimen the strain-rate drops from -0.1 s^{-1} to -0.03 s^{-1} in this particular case.

The global specimen failure occurs between 4 mm and 5 mm plunger displacement after which high strain-rates occur. Figure 5.25a indicates a reduction in strain-rate and stress of element A at 2.5 mm displacement, which is next to the plunger interface. At this point first elements fail, which can affect the backing of other elements and the global stress distribution. In compression, several elements may fail relatively long before the global specimen failure, unlike in tension, where a couple of failed elements suffice to initiate global failure (see Figure 5.23). In tension, the stress and strain increase is continuous until the global failure. In compression, the failure of elements (partly significantly) before the ultimate failure leads to a re-distribution of load (stresses) to the remaining elements. After first elements fail this continues and repeats until ultimate failure and gives Figure 5.25b the slightly unsorted appearance.

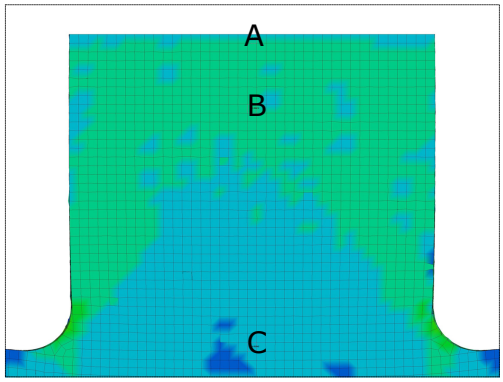

Figure 5.24. Compressive numerical specimen and selected elements for strain-rate analysis.

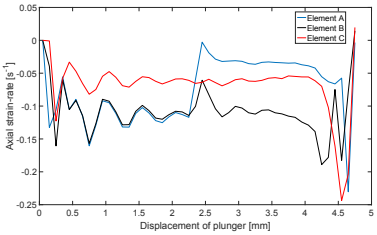

a Compressive strain-rate over plunger displacement for three different elements.

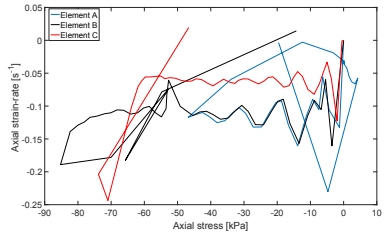

b Compressive strain-rate over stress for three different elements.

Figure 5.25. Strain-rate in a numerical specimen under compression with reference to element locations shown in Figure 5.24.

The stress-strain relationship for the elements at the impact interface (element A, compression) and the failure (Element C, tension) is displayed in Figure 5.30 (following Section 5.5), where the stress values are used for an assessment of viscous strain.

In bending the strain-rate of elements is presented in their variation over length (Figure 5.26a) and through thickness (Figure 5.26b). Additionally, the strain-rate of an element in the center at the top of the beam (near the failure) is compared to one near the root, where notch effects occur (Figure 5.29). Figure 5.27 indicates the slightly higher stresses occurring near the notch (Element N) compared to the middle (Element C).

Figure 5.27a shows that the stress strain-rate behavior of one of the three elements on the top surface is qualitatively similar with increasing stresses towards the root. The variation in the strain-rate is related to the gradual transition from the elastic to the plastic regime of the different layers. The failure initiations starts near Element N (Figure 5.26a) and the opposite side,

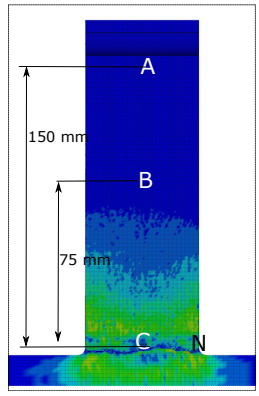

a Cantilever beam and selected elements over length for strain-rate analysis.

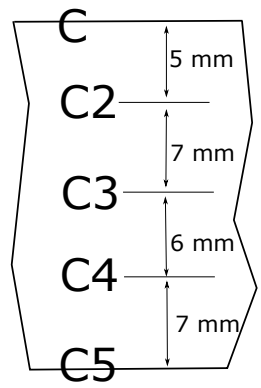

b Elements through thickness selected for strain-rate analysis. The elements C2 - C5 are in the same lateral location as element N (Figure 5.26a).

Figure 5.26. Elements selected for analysis in the cantilever beam.

which leads from a stress of $\tilde{1}20$ kPa to an increase in strain-rate as the load carrying cross-section on top extenuates. This sudden increase in strain-rate is also found in Element C2, onces the layer with element above it fails and the load is redistributed. The same effects are shown in Figure 5.27a, where the strain-rate is plotted over the plunger displacement.

Figure 5.27b shows the stress and strain-rate relationship through thickness. As the top-layers are of higher strength (see also Figure 5.6) the neutral axis closer to the top; consequently, the deformations (Figure 5.28a) and strain-rates at the bottom are higher than at the top. As soon as the first top layers fail the strain and its rate increase suddenly 5.27b.

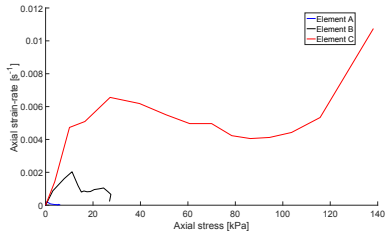

a Strain-rate on the top of a cantilever beam over plunger displacement for three different elements

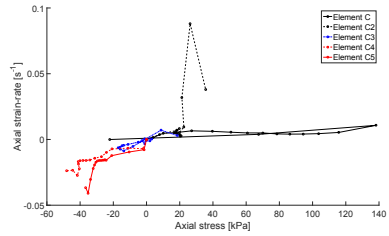

b Strain-rate through thickness of a cantilever beam over stress

Figure 5.27. Strain-rates in a cantilever beam.

The average tensile strain-rate is around 0.05 s^{-1} and in compression its absolute value is slightly higher. Peaks or sudden changes refer to the failure

of the top layers.

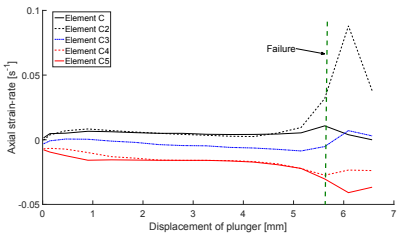

a Strain-rate through thickness of a cantilever beam over plunger displacement

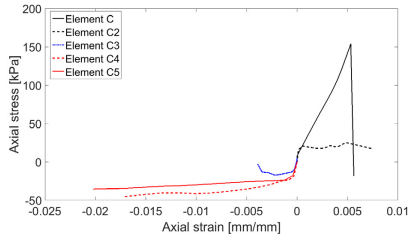

b Stress-strain relationship through thickness of a cantilever beam

Figure 5.28. Strain-rate progress through thickness of a cantilever beam.

Figure 5.28b shows the stress-strain distribution through thickness of elements close to the later crack (see Figure 5.27a). A comparison of the stress distribution through thickness for the numerical model and the analytical homogeneous model of ITTC (2002) is found in Figure 6.1. The strain-rate at the edge near the notch is around three times higher than in the center, i.e., 0.015 s^{-1} (Figure 5.29). On the top of the cantilever beam the strain-rates can reach the same order of magnitude as in the tensile tests, but their absolute values are in all cases lower than those in tension or compression [13].

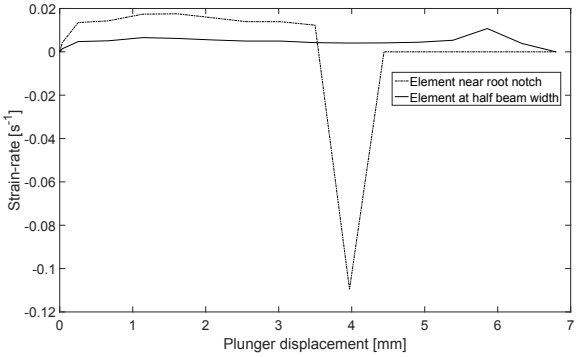

Figure 5.29. Strain-rate development on the top of the cantilever beam at the center (C) and the outer edge near the root notch (N).

The strain-rates in compression and tension are in the same order of magnitude; therefore, strain-rate effects are not considered causative for different stiffness in compression and tension, but as a material inherent property. In bending the strain-rate is approximately one order of magnitude lower than in tension and compression (see Figure 5.28). The activation of viscous effects is associated with a more compliant response at lower strain-rates. This,

[13] This topic is also addressed in the discussion Section 7.2.

however, is not the case here; consequently, the through thickness distribution (PIII) of properties appears to be a valid explanation for the *apparently higher stiffness* in bending compared to uniaxial tensile tests.

5.5 Application of Viscous Theory on Model-Scale Ice in Compression

Sea ice undergoes, in compression, elastic deformation in addition to delayed (visco-) elastic and visco-plastic deformation. The viscous deformations are strain-rate dependent (e.g. Sinha, 1978b, 1982; Sanderson, 1988; Timco and Weeks, 2010). As indicated in PII and Table 5.1, the hardening modulus or the effective strain modulus is around 1% of the elastic modulus. Consequently, the tested specimens undergo relatively large strains (Figure 5.30 shows the compressive stress-strain curve of Element A) [14] to which comparisons with sea ice are made.

The visco-elastic strain is defined by Equation 5.15 where C is a constant ($9{\cdot}10^{-3}$ m) for pure ice and α_T is a temperature dependent quantity with related to -10 C°. Both parameters are also used in the calculation for model-scale ice, as equivalences for model-scale ice are unknown. The elastic modulus is 148 MPa (Table 5.1), the grains size, d, is rounded to 1 mm and the deformation time, t, to 1 second. The exponent, q, is according to Sanderson (1988) 0.34, but may also be the reciprocal of the exponent, n, in Norton's law Sanderson (1988) [15] for the secondary creep, which is 3. However, related to experiments with granular polycrystalline ice an approximate value of $n = 5$ and $q = 1/5$ (Jones, 1982; Moores et al., 2001) is considered more appropriate. The compressive stress 85 kPa refers to the stress in Figure 5.30. This delivers a delayed elastic strain of 0.0009. Compared to the strain 0.075 in Figure 5.30, this value would be around 1 % of the total strain [16].

$$\epsilon_d = \frac{C\sigma}{Ed}(1 - exp[-(\alpha_T t)^q]) \tag{5.15}$$

The secondary creep, see Section 3.1, represents strains referring to plastic deformation. Sanderson (1988) presents the formulation for granular sea ice which accounts for the porosity of sea ice. The porosity, por, in the model of the model-scale ice and in the numerical model is 5 %, which is accounted for

[14] Note: this element does not fail, but is close to a failing element.

[15] It originally refers to the creep of steel at high temperatures, but is also used in other disciplines such as rock mechanics (e.g., Bürgmann and Dresen, 2008) and for super-alloys (e.g., Golan et al., 1996).

[16] An alternation of the exponent, n, would not change the magnitude of the result.

in Sanderson (1988) (Equation 4.10), which results in 5.16. However, as the stresses in Figure 5.30 result from a model, where porosity is already accounted for, $1-por = 1$ is used. The parameters in Equation 5.16 are constants related to the crystal type, (g = granular) $A_g = 7.8{\cdot}10^{16}$ MPa^{-3} s^{-1}, the activation energy, $Q_g = 120$ kJ / mol, the universal gas constant, $R = 8.314$ J / mol K [17], the temperature in Kelvin, $T = 273$ K, and σ the stress from Figure 5.30 as 50 kPa and 85 kPa for the failed element. The universal gas constant relates the energy scale (unit in Joules) to the temperature scale of a particle (mole) to which the activation energy, Q, also refers.

An integration over time (deformation time approximately 1 second) of Equation 5.16 would deliver a viscous strain of approximately 2.7 $\cdot 10^{-13}$ s^{-1} and 3.8 $\cdot 10^{-12}$ s^{-1} respectively. A continued discussion of this topic is found in Section 7.2.

$$\dot{\epsilon} = A_g \left[exp\left(\frac{Q_g}{RT}\right)\right] \left(\frac{\sigma}{1-por}\right)^n \tag{5.16}$$

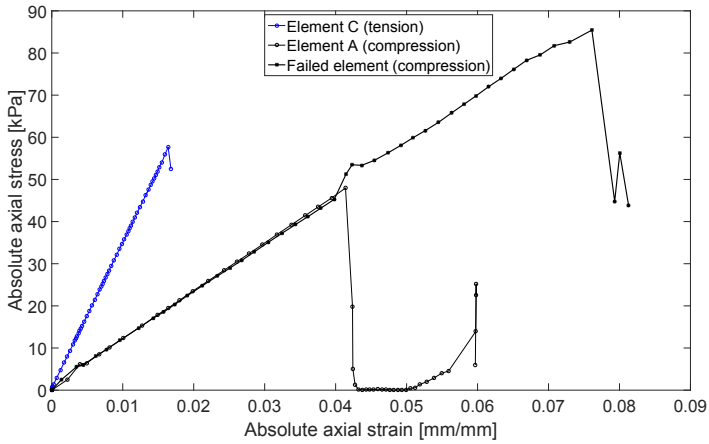

Figure 5.30. Stress-strain curve elements in numerical specimens in compression. Element C refers to Figure 5.23a and Element A refers to Figure 5.25 and the failed elements are withing the later failure pattern (e.g., Figure 5.20).

The curves in Figure 5.30 reflect that the lower strains and higher stress increase in tension rather than in compression. This already manifests in the force-displacement curves and the higher strain modulus (hardening modulus) used (see also Figure 5.28b).

In compression Element A does not fail, but first elements around Element A fail, which takes away supporting elements of Element A; consequently, only small stresses and deformations are acting on the element. The failed element

[17] R is an equivalent to the Boltzmann constant.

lies within the global failure pattern of the specimen (e.g., Figure 5.20) and is consequently one of the last elements to fail. This element also shows a stress increase at the point where the stress drops in Element A. Due to the failure and stress-relaxation of some elements, the stresses are redistributed to the load-carrying elements. In compression, several elements fail already before the global failure of the numerical specimen. In tension, however, the failure of the first elements causes instant global failure of the specimen. Element C does not fail itself and is plotted here until the point where the numerical specimen fails globally.

5.6 Summary and Main Findings

The cantilever beam test simulation, with the values compiled in Table 5.1 is presented in Figure 5.31, together with experiments. The failure force refers to the ITTC bending strength of 59 kPa. The model accounts for hydrostatic buoyancy and tip flooding forces [18].

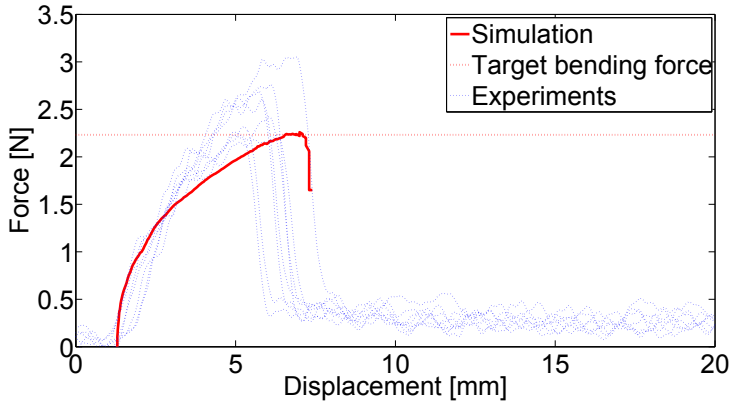

Figure 5.31. Simulation and experiments of the cantilever beam bending (PIII).

The functionally graded model for the cantilever beam maintains compliance with the uni-axial tests [19] and indicates two significances that occur in bending. First, the model-scale ice must be modeled as a functionally graded material which is of significant strength on top compared to the lower layers. Secondly, in bending, layers that are close to the neutral axis respond elastically and

[18] The water density used is 997 kg/m^3. The force-displacement curve and von Mises stress distributions of the numerical model at various stages is found in Appendix C.1.

[19] With some limitation in compression (see Figure 5.9 and Figure 5.17).

others plastically, whereas the plastic region grows from the outer layers with the increasing load, which has a strong impact on global specimen stiffness (Figure 5.32).

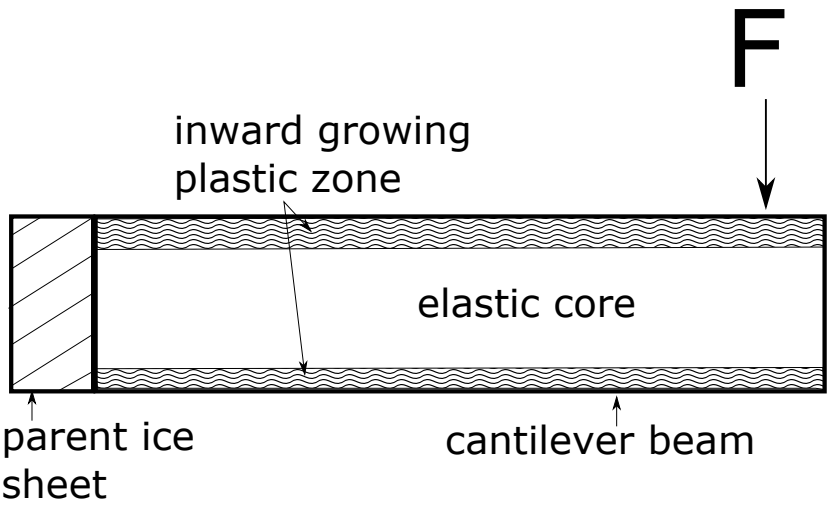

Figure 5.32. Principle sketch of the material behavior of a cantilever beam of model-scale ice under load, F, with adjacent ice sheet. The increasing load causes a growth of the plastic zone from the outer edges inwards, towards the center.

The average strain modulus [20] in bending is one order of magnitude greater than the one based on the uni-axial tensile tests [21] and one order of magnitude smaller than the elastic modulus (Figure 5.33).

[20] This is the modulus representing the stress-strain relationship.

[21] The hardening modulus in compression is 1.14 MPa and even lower than the one for tension (3.07 MPa).

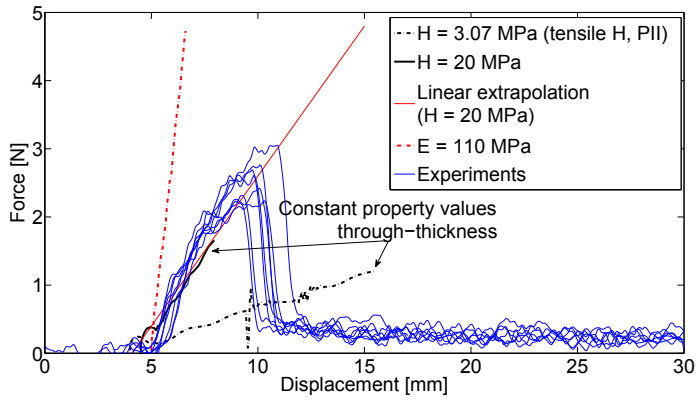

Figure 5.33. A visualization of the beam bending experiments and numerical models (PIII with additional explanations). The model based on the uni-axial tensile tests has a stiffness significantly lower than the experimental results. A model with constant properties through thickness that complies with the average stiffness of the experiments (red solid line) requires a hardening modulus that is one order of magnitude higher (H $\approx$ 22 MPa).

6. The Scalability of Model-Scale Ice Properties and Model Testing [PIII, PIV]

In the following, the scalability of the model-scale ice of the Aalto ice tank is discussed on the basis of the found mechanical behavior. Scalability means in this context the capability of the model-scale ice to be scaled, respectively, to comply with requirements set by the state of the art scaling laws following Froude and Cauchy similitude.

6.1 A Review of the State of the Art Scaling Approach

This section provides a brief review on the scaling approaches used in model ice. The state of the art refers to geometric scaling while maintaining Froude (Equation 1.1) and Cauchy number (Equation 1.2) in both scales. The Cauchy number represents the ratio between inertial forces, applied by the momentum of the ship, and the elastic response-forces of the material, i.e. the ice. Consequently, Cauchy similarity is only valid at sufficiently high ship speeds, as at low impact speeds inertial forces are small (see, e.g. Schwarz, 1977; Palmer et al., 2009. Furthermore, the ice must be loaded at sufficiently high strain-rates ($\geq 10^{-}3$) to be considered as responding elastically until failure (see, e.g. Derradji-Aouat, 2010). Therefore, the response in model-scale is aimed at being elastic for ship-ice interactions as well.

In the following, the origin of Froude number, Fn, and the Cauchy number, Ch, is shown on the basis of Vance (1975); Zufelt and Ettema (1996). As found in Vance (1975); Atkins (1975); Zufelt and Ettema (1996); Palmer (2008) it is set that the factor λ scales the length dimension, L, between model (subscript m) and prototype (subscript p, Equation 6.1), while $\sqrt{\lambda}$ scales the time dimension, T, in Equation 6.2.

$$\frac{L_p}{L_m} = \lambda \tag{6.1}$$

$$\frac{T_p}{T_m} = \sqrt{\lambda} \tag{6.2}$$

Inertial forces, F_i, gravitational forces, F_g, and elastic forces, F_e, are defined in Equation 6.4 (Vance, 1975) with the mass, M, density, ρ, volume, V, gravitational acceleration, g, acceleration, a, area, A, elastic modulus, E, stress, σ and strain, ϵ.

$$\begin{aligned} F_i &= Ma &&= \rho V L T^{-2} \\ F_g &= Mg &&= \rho V g \\ F_e &= \sigma A &&= E\sigma\epsilon \end{aligned} \tag{6.3}$$

The Froude similitude is applied when inertial forces and gravitational forces are significant, i.e., when ice is accelerated by the transferred momentum of the ship and submerged (see, Vance, 1975) until gravitational forces restore its floating position. Froude similitude may be considered valid for many ship-ice interaction scenarios. However, at low interaction speeds, such as civil structures versus slowly drifting ice sheets, inertial forces play an insignificant role (see also, Atkins, 1975; Palmer et al., 2009).

The relationship between inertial forces and gravitational forces and the resulting Froude number is found in Equation 6.5 with the velocity, v, defined as $v = LT^{-1}$.

$$\begin{aligned} \frac{F_{i,p}}{F_{g,p}} &= \frac{F_{i,m}}{F_{g,m}} \\ \frac{\rho_p V_p L_p T_p^{-2}}{\rho_p V_p g_p} &= \frac{\rho_m V_m L_m T_m^{-2}}{\rho_m V_m g_m} \\ \frac{L_p T_p^{-2}}{g_p} &= \frac{L_m T_m^{-2}}{g_m} \\ \frac{L_p}{g_p T_p^2}\frac{L_p^2}{L_p^2} &= \frac{L_m}{g_m T_m^2}\frac{L_m^2}{L_m^2} \\ \frac{v_p^2}{g_p L_p} &= \frac{v_m^2}{g_m L_m} = Fn^2 \end{aligned} \tag{6.4}$$

In the icebreaking process, the momentum (inertia) of the ship interacts with the ice. The ice is broken and the broken floe is accelerated, which can also involve significant added mass effects. On the basis of sufficiently high strain-rates ($\geq 10^-3$, see, e.g. Sanderson, 1988; Derradji-Aouat, 2010), the ice responds elastically until failure (Vance, 1975). Cauchy similitude (Equation 1.2) represents the ratio between inertial and elastic forces and may be applied

when the deformation process on both scales is governed by elasticity. The derivation of the Cauchy number, Ch, is demonstrated in Equation 6.6, on the basis of Equation 6.4, 6.1, 6.2.

$$\begin{aligned}
\frac{F_{i,p}}{F_{e,p}} &= \frac{F_{i,m}}{F_{e,m}} \\
\frac{F_{i,p}}{F_{i,m}} &= \frac{F_{e,p}}{F_{e,m}} \\
\frac{\rho_p V_p L_p T_p^{-2}}{\rho_m V_m L_m T_m^{-2}} &= \frac{E_p \epsilon_p A_p}{E_m \epsilon_m A_m} \\
\frac{\rho_p}{\rho_m}\lambda^3 \frac{L_p T_p^{-2}}{L_m T_m^{-2}} &= \frac{E_p}{E_m}\lambda^2 \\
\frac{\rho_p}{\rho_m}\lambda^3 \frac{L_p T_p^{-2}}{L_m T_m^{-2}} \frac{L_p}{L_p} &= \frac{E_p}{E_m}\lambda^2 \\
\frac{\rho_p}{\rho_m}\lambda^3 \frac{v^2}{v^2}\frac{1}{\lambda} &= \frac{E_p}{E_m}\lambda^2 \\
\frac{\rho_p v_p^2}{E_p} &= \frac{\rho_m v_m^2}{E_m} = Ch
\end{aligned} \tag{6.5}$$

6.2 The Scalability of the Bending Strength [PIV]

6.2.1 The Functionally Graded Model

Normally, the bending strength is an analytically calculated stress referring to an isotropic and homogeneous material with its neutral axis in the center at half thickness, as proposed by ITTC (2002). However, as elaborated in PIII and displayed in Figure 5.6 the strength properties are not constantly distributed over the thickness, but are functionally graded through thickness. Figure 6.1 compares the stresses of the numerical model of PIII and the stresses of a model-scale ice beam with homogeneously distributed properties. The corresponding stresses of the numerical model are based on the stress outputs of five different elements at different locations over thickness. Figure 6.1 indicates a significant disagreement between the two models, despite equivalent failure force.

The assumption of isotropy and homogeneity on sea ice is also applied in full-scale measurements (e.g., Krupina and Kubyshkin, 2007; Suominen et al., 2013). Kerr and Palmer (1972) proposed functions for the distribution of the elastic modulus over thickness in sea ice, which found successful application in e.g. Åse (2013); Ehlers and Kujala (2014) for numerical and analytical remodeling of experiments (Kujala et al., 1990). In all cases, the reference

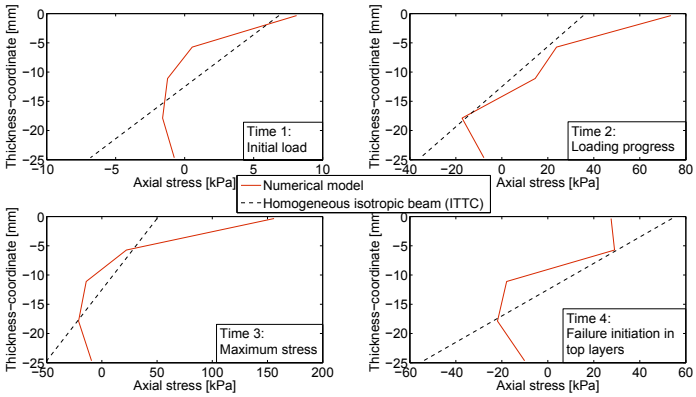

Figure 6.1. Stress distribution in the model-ice cantilever beam based on the numerical model of PIII and the analytical homogeneous material model proposed by ITTC (2002).

measurements were taken in winter. On a macroscopic level, the gradient of the stiffness properties in sea ice is less than in model-scale ice (compare e.g., Kerr and Palmer, 1972 or Ehlers and Kujala, 2014 with PIII).

6.2.2 The Temperature Variation Though-Thickness

The ice is a boundary layer between the relatively warm water and the cold air. In model-scale this boundary layer is thin, so the temperature change has to take place over a considerably thinner layer, which leads to a stronger gradient. In addition to the temperature gradient at the time of testing (PIII) the time-history of the cooling process with the low temperature in the consolidation phase might also affect the gradient of the through-thickness properties of the model-scale ice. Table 6.1 states that the C°/m gradient, especially in the production phase of the model-scale ice, is very high. This might be the main cause of the significant strength property gradient in the model ice. Table 6.1 compares the temperature difference over thickness for the Aalto model ice sheet analyzed in PI-PIII and sea ice data from Petrich and Eicken (2009) taken in the year 2008 in Barrow.

6.2.3 A Simplified Numerical Example on the Impact of Different Property Distributions

The different distributions of properties in model scale and full scale lead to different positions of the neutral axes and, consequently, different tensile stresses on top. A numerical example calculation is performed comparing the bending strength for a property distribution of sea ice (Kerr and Palmer,

Table 6.1. Temperature distributions in sea ice and model-scale ice.

		Model ice		Sea ice Petrich and Eicken (20	
		Production phase	Testing	February 2008	May 2008
Temperature	Top [C°]	-12	-0.9	-16	-4
	Bottom [C°]	-0.3	-0.3	-2	- 2
Thickness [m]		0.025	0.025	0.9	1.4
Linear gradient [C°/m]		-480	-24	-18	-1.4

1972), model-scale ice (PIII) and ITTC, while assuming that materials respond elastically, as it might occur in rapid ship-ice interactions (see Figure 6.2). The materials in this example are set to have the same bending strength (following ITTC, 2002), i.e. the same load (2 N), at failure for beams of equivalent dimensions (170 mm length, 58 mm width, 25 mm thickness).

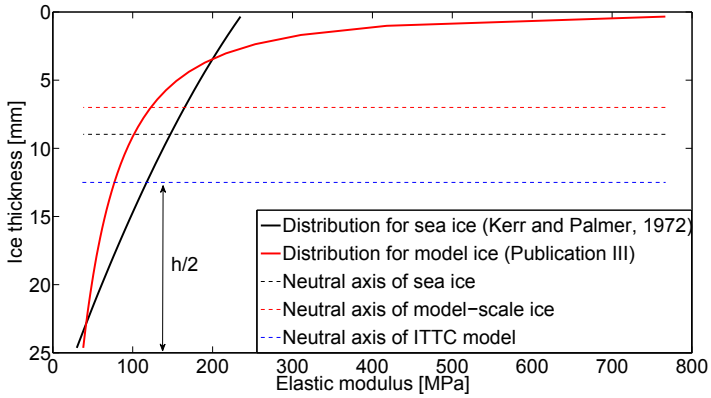

Figure 6.2. Elastic modulus distributions and the related neutral axis for model ice and sea ice (scaled) in a 25 mm thick ice sheet with the model of ITTC as reference.

The stresses in the top layer, σ_x, are calculated using the bending moment, M_b, the area moment of inertia, I, and the distance between the top layer and neutral axis, za, according to Equation 6.6.

$$\sigma_x = \frac{M_b}{I} za \tag{6.6}$$

The results according to Equation 6.6 are compiled in Table 6.2. The deviation between the model with constant properties through-thickness and the functionally graded distributions for sea ice and model ice are significant [1]. The different strength distributions indicate that the bending strength, specifically the axial tensile strength on top, is not scaled with the simplified

[1]It is acknowledged that environmental conditions and thickness affect the gradients and hence this example can only be an indication of the qualitative differences.

standard methods. The neglecting of differences in the material constitution between both scales effectively scales the response force level in a specimen with geometrically scaled dimensions, but not necessarily the flexural stress.

Table 6.2. Data of analytical example calculation on stresses in a cantilever beam.

	ITTC model	Sea ice	Model ice
Stress, σ_x [kPa]	56	41	32
Deviation from model with constant properties through-thickness	0 %	27 %	43 %

6.3 Scalability in Perspective of the Material Stiffness [PI - PIV]

The flexural strength (according to ITTC, 2002) is significant to assess the strength properties of level ice is an important index.

Another material parameter of significance for loading at high strain-rates is the elastic modulus, E, as it contributes to the bending stiffness and is indirectly a measure for the critical displacement of a cantilever beam at failure. A material of low rigidity, consequently, requires more work to be bent until failure, as the required failure strain is higher than for stiffer materials (see, Schwarz, 1977 and Equation 6.7).

$$\frac{E_{full\ scale}}{\sigma_{b,full\ scale}} = \frac{E_{model\ scale}}{\sigma_{b,model\ scale}} \geq 2000 \tag{6.7}$$

If the elastic modulus of the ice sheet being investigated in this thesis were the dominant material parameter, the ratio $\frac{E}{\sigma_b}$ would be 1864 (see Equation 6.9) and close to the postulated target value of Schwarz (1977) (Equation 6.7). However, in order to obtain a force-displacement curve of a similar progression as in the cantilever beam experiments, the stiffness would need to be equivalent to an elastic modulus of around 15 MPa, which is visualized in Figure 6.3.

As the response in bending is a mixed response of elastic and plastic domains, the material property is, consequently, not named the elastic modulus, as in Figure 6.3, but an equivalent stiffness, S_{equ}, of 15 MPa, which is used to calculate the ratio with the flexural strength in Equation 6.9.

$$\begin{aligned} \frac{E}{\sigma_b} &= \frac{110\ MPa}{59\ kPa} = 1864 \\ \frac{S_{equ}}{\sigma_b} &= \frac{15\ MPa}{59\ kPa} = 254 \end{aligned} \tag{6.8}$$

The elastic modulus determined by the plate deflection method (PI) is considered to be the actual elastic modulus, which is effective until a low yield

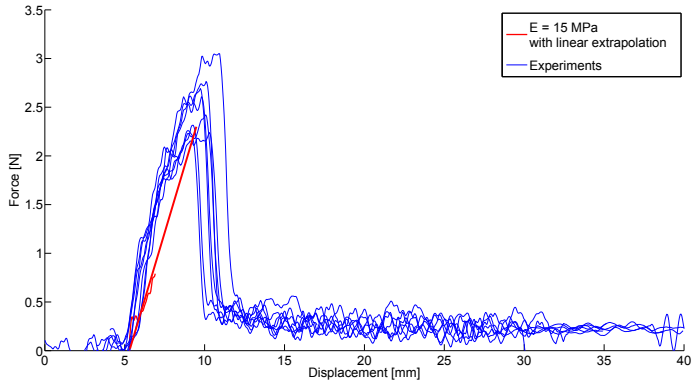

Figure 6.3. Cantilever beam experiments together with a linear-elastic simulation of the cantilever beam.

stress (PII). In PIII it is shown that in bending the outer layers respond plastically, whereas those closer to the neutral axis respond elastically. Because of this, the elastic modulus determined by cantilever beam tests (see, e.g., von Bock und Polach, 2005) would deliver a lower value than the deflection of an *infinite plate on elastic foundation*. A significant difference between these two methods was also stated in Enkvist and Mäkinen (1984); Evers and Jochman (1993).

Figure 6.4 shows the force-displacement curves of two numerical cantilever beam experiments. The experiment is conducted once with a linear elastic cantilever beam using the elastic modulus measured in the experiments (PI), by the deflection of an infinite plate; the second simulation uses the numerical model developed on the basis of the damage model of (PIII). The indicated maximum bending force in Figure 6.4 represents the target bending force at which the cantilever beam has to fail in order obtain a bending strength of 59 kPa, according to ITTC (2002).

The integration of the area below the curves in Figure 6.4 up to the maximum bending force reflects the work required to break the cantilever beam (Figure 6.5). The energy expended in the elasto-plastic model representing the experiments is here ≈11 times greater than in the linear elastic case. In conclusion the model ice may represent the response force correctly, but the energy required to break the ice is too large [2]. This may reduce the scalability when the energy of the ice-breaking process is of significance and other effects do not compensate for *the icebreaking energy* being too high in model-scale.

[2]Based on the assumption that the ice should be represented as linear-elastic material.

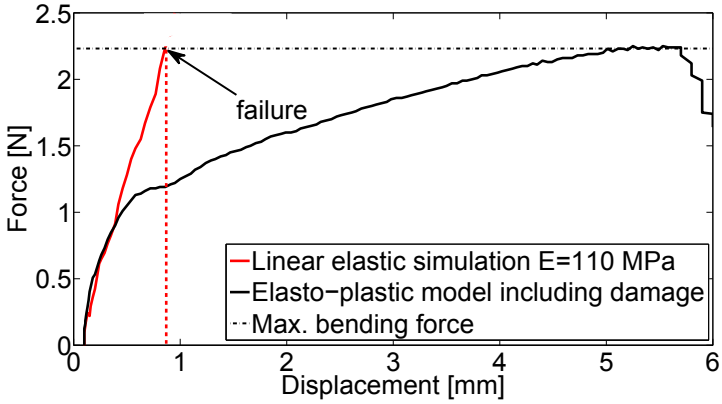

Figure 6.4. Numerical cantilever beam experiment with a linear-elastic material and an elasto-plastic material including damage and through-thickness dependent property distributions (PIII).

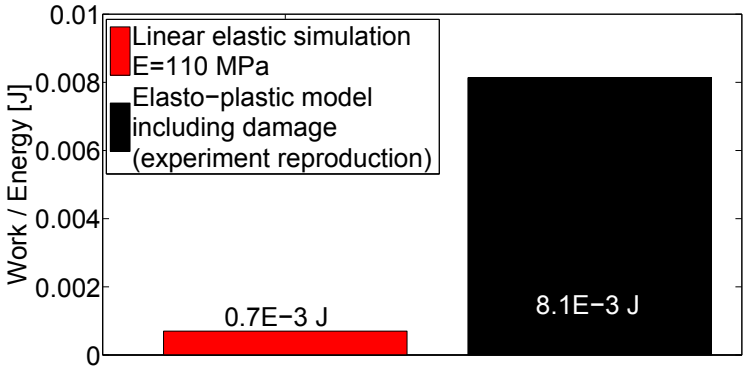

Figure 6.5. Energy expended in the numerical cantilever beam experiments.

6.4 The Impact of Experimental Differences on the Scalability

Independently from the applied scaling laws, the transfer of information, or the scaling of data between model scale and full scale, is affected by the characteristics of tests. The bending strength is tested in model testing basins mainly by cantilever beam tests following the standards of the ITTC (2002). However, the notch effect at the transition between beam and its root amplifies stresses, the impact of which is already shown by Svec et al. (1985). In full scale the bending strength is determined by cantilever beam tests (e.g., Krupina and Kubyshkin, 2007), three point bending tests (e.g., Suominen et al., 2013) or four point bending tests (e.g., Kujala et al., 1990). Both finite element, FE, simulations in PIV with the model of Ehlers and Kujala, 2014 and measurements of Kujala et al. (1990) reported significantly higher bending stresses at

failure in four point bending experiments than in cantilever beam experiments. The axial stress at failure in the cantilever beam is found to be 37% lower compared to the four point bending test. This is an additional aspect that might limit the scalability, especially when the bending strength on test voyages is determined with a different method than in model scale.

7. Concluding Remarks

7.1 Conclusion

The thesis presents a numerical model of the strength and deformation behavior of the model-scale ice of the Aalto Ice Tank. The model is valid for tension, compression and downward bending. The numerical model provides valuable insight into the mechanical behavior of the model-scale ice and is a substantial step towards a numerical ice tank.

The experiments included uniaxial tensile and compressive specimen tests as well as downward cantilever beam tests. The testing of the tensile specimens is a new approach (PI) which is not even covered by the ITTC (2002) guidelines. The tensile tests provided essential information on the mechanical behavior of model-scale ice and supported the development of the numerical model significantly. Furthermore, both the tensile testing method and the information on tensile strength already attracted the attention of other ice tanks with the potential of a growing impact in the future.

The numerical model is built of finite elements which are modeled on grain size level and includes randomly distributed flaws, which represent the inclusions of air and water [1]. An analysis conducted in PII shows that the flaws have an impact on the failure pattern, which made it possible to reproduce variations in the failure patterns that were observed in the experiments. Especially in tension, a variation of flaw distribution can partially explain variations in response forces, but not in full.

The elastic modulus is experimentally determined by the deflection of an infinite ice sheet on an elastic foundation. The encountered non-elastic deformations at low loads (compared to uniaxial or flexural tests) and its analysis indicated that for a homogeneous model-ice material the yield strength is lower

[1] The water includes ethanol.

than 1 kPa PI. In the plastic domain, after yielding, the strain modulus in tension and compression is less than 3% of the elastic modulus, i.e. two orders of magnitude lower. Consequently, the measured loads or stresses refer to significant deformations or strains.

The assumption of constant properties through thickness would require, in bending, a strain modulus being one order of magnitude larger than in uniaxial tension or compression to reproduce the experiments. The modeling of the cantilever beam tests (PIII) require a functional grading of the elastic and tensile properties through-thickness. The functional grading of properties also complies with experimental observations, where the top of the model ice appeared to be of higher strength than the bottom. As the top layer yields early, the strain modulus in the plastic regime (i.e. named *hardening modulus*) requires a significantly higher stiffness than the average stiffness [2]. Due to the through-thickness distribution of properties, the outer layers of the model-scale ice responds after short loading time plastically, while the core remains in the elastic regime. Consequently, the elastic modulus determination on the basis of the deflection of an infinite plate deliver a different result than the one [3] on the basis of cantilever beam tests, as it refers to a mixed response of an elastic and a plastic domain. This insight is considered of high value for the ice model testing community as the difference between the methods has also been noted by other facilities (see Enkvist and Mäkinen, 1984; Evers and Jochman, 1993). The through-thickness distribution is an essential parameter to represent tensile, compressive and downward flexural behavior in one model. The low yield strength and the significant difference in stiffness between the elastic and the plastic domain cause different macroscopic response stiffnesses in uniaxial loading and flexural loading. In uniaxial loading the specimen responds fully plastically, whereas the response in bending is a mixture of plastic responses (outer layers) and elastic responses (inner layers, close to the neutral axis).

An analysis of the strain-rates in the three different loading cases did not point to a significant presence of strain-rate effects or viscous strains.

As the model-scale ice is found to yield early (PI and PIV), Cauchy-scalability cannot be fulfilled. In ship-ice interaction ice is usually loaded until ultimate failure, which reduces the significance of the response being dominated by an

[2]This is equivalent to the properties constant through thickness.

[3]Strain modulus would be the correct term, but elastic modulus is commonly used in this context.

elastic modulus or another strain modulus, as long as the consumed deformation energy for sea ice and model-scale ice is equivalent. Consequently, in the Cauchy similitude the elastic modulus should be replaced by the effective strain modulus, which can be determined by cantilever beam tests [4]. This effective strain modulus has to replace the elastic modulus in the E/σ_b ratio. In model-scale and full-scale it is best practice to calculate flexural stresses based on the assumption of homogeneity and isotropy for the properties through thickness. In both scales the functional grading of the properties is different over thickness, in consequence, the assumptions of invariant properties through thickness effectively scales the response force, but not the failure stresses. This may be an explanation as to why ice resistance tests show reasonable scalability, despite the pronounced plasticity of the model-scale ice. However, this may also restrict the scalability to certain scenarios and can cause a poor representation of certain ice resistance parts (see also (Vance, 1975)).

This thesis provides unique insight into the mechanical behavior of model-scale ice in combination with a numerical model. The gained insight into the mechanical behavior also provides a basis to discuss the scalability of the model-scale ice.

7.2 Discussion and Future Work

The work presented uses an elasto-plastic damage model to represent the material behavior of the Aalto model-scale ice. The experiments and numerical model for model-scale ice presented in PI, PII and PIII are only valid for a thickness of 25 mm and a bending strength of 59 kPa (according to ITTC, 2002). Consequently, the experiments presented in PI should be repeated for different bending strength to thickness relationships in order to gain a more global understanding of the mechanics of model-scale ice. Furthermore, similar experiments should be commenced by other ice model tanks to assess the differences between various model ice types [5]

The numerical model contains voids that are explicitly modeled and distributed randomly. The variation of the maximum response forces in the

[4] This is valid for ship-ice interactions, where the bending is the main deformation mode.

[5] On the basis of PI and PII experiments conducted as in this thesis are already planned by other facilities.

simulations is shown as a function of the amount of voids and their void locations (see Section 5.3.7 and PII). An increasing number of voids weakens the material and reduces the response force. The variation of the void-locations affects the maximum force in compression less than in tension (± 6 %). This can partly explain the variation in response forces in the experiments, but not in full. It remains to be investigated, whether the variation in response force may be related to high local void density variations or other reasons [6]. Especially in compression, the variation of the voids causes variations of failure patterns that were also observed in the experiments (see PI, Figure 4.9 and Figure 5.20). The variation in response resulting from varied random flaw distributions is indicative and not exhaustive, as the number of possible versions is naturally very large. In the experiments a notable, but not significant, variation in response stiffness is found, which is accounted for by different hardening moduli (i.e. strain moduli) in the numerical model (PII).

Each uni-axial experiment is reproduced numerically, while varying specimen dimensions refer to different void distributions. Consequently, the random void distributions transfer an uncertainty to the determined critical damage, dc, values. However, the variation in failure pattern in the experiments (see PI and Figure 4.9) indicate that already the physical model ice and the experimental results were subjected to a variation of the void distributions. Therefore, the values presented in Table 5.1 are affected with uncertainty, but are considered to be good guiding values.

The experiments and related simulations provide information or indications on boundary values for most tensile property distributions. Significantly less information can be derived for the compressive properties; consequently, the compressive hardening modulus and the compressive yield strength are kept constant through-thickness (Table 5.1). The compressive yield strength is treated as the only wild-card parameter, which is defined to achieve compliance of the cantilever beam simulation with the experiments. Its rather high value (see Table 5.1) compared to the model, where properties are constant through thickness (Table 5.1) causes an offset in displacement for the force-displacement curves of the functionally graded material (see Figure 5.9). It might be possible to overcome this with an appropriate grading of properties through thickness, however this requires additional information on possible distributions. Furthermore, its value may also reflect shortcomings in modeling assumptions of other parameters. Consequently, in the functionally graded

[6] Local changes in void density can affect the response stiffness of a specimen.

model the compressive yield strength is partly to be seen as corrective, but also as indicator that additional research is required on this topic.
At this point it is unknown, whether the modeled *plastic domain* reassembles other sub-domains which might refer to strain-rate sensitive effects. A calculation of strain-rate related strains (Section 5.4) points to them being less than 1% of the total strain. However, the formulations and constant values applied partly refer to sea ice, as their equivalences for model-ice are unknown. The strain-rates in compression and tension are in the same order of magnitude and those in bending are lower. However, the commonly associated decrease in stiffness with decreasing strain-rates is not observed. Consequently, differences in stiffness for tension, compression and bending are not considered to refer to strain rate effects but rather to material anisotropy and functional grading of material properties (Sanderson, 1988; Schulson, 1999; Moores et al., 2001). The functional grading of the material and the combined response of elastic and plastic layers appears to be an acceptable explanation for the increased stiffness encountered in bending. In all experiments the time elapsed between load initiation and failure was 1 second or less, which is considered too short to significantly activate viscous effects [7]. However, the currently available knowledge on the strain-rate sensitivity or viscous behavior of model-scale ice is very limited and should be addressed in the future, experimental research, especially for strain-rates being significantly lower than those in this thesis.
Experiments in other ice sheets show that the nominal compressive pressure increases with decreasing area of the impact face (see PIV) by 10% to 20%. In PIV it is shown that the model of PII cannot reproduce this effect and consequently more research and dedicated experiments are required in the future to investigate the compressive properties of the model-scale ice. Consequently, in future compressive experiments are to be conducted with different specimen geometries and different ice strength, i.e. bending strength, to assess the impact of through thickness property variations in connection with varying specimen geometries. As a consequence of the research presented in this thesis the latter will be investigated jointly by Aalto University and HSVA in the Horizon 2020 EU project *HYDRLAB-PLUS* (Project ID: 654110).

The functional grading of the material properties is considered a result of differences in the boundary conditions of the surrounding temperature (see also e.g., Gow and Ueda, 1989). In PIII the temperature gradient at the

[7] The loading rate in the experiments complies with the recommended procedures of ITTC (2002).

time of the measurements is considered as cause for the property variation through-thickness. However, it remains to be clarified how significantly the temperature gradient in the production process (see Table 6.1) affects the ice properties. The presence of the strong gradient is considered as valuable insight for the design of new production processes for the model-scale ice of the *Aalto Ice Tank*.

The non-compliance of the model-scale ice with Cauchy similitude and the target E/σ_b ratio requires a review of the actual practical feasibility of this scaling approach. With reference to Atkins (1975); Palmer et al. (2009) and Jordaan et al. (2012) it is considered worthwhile to investigate the feasibility of alternative scaling approaches, where different scaling methods are applied to different scenarios, i.e. case-based scaling.

The model in this dissertation indicates how to combine information from several independent tests, and explains the differences between the elastic modulus and the stiffness in bending. The bending stiffness was, however, lower that desired, which requires experimental research to raise the material stiffness in bending and to reduce, eliminate or strengthen the weak plastic domain for ship-ice interactions.

This thesis intends to be the corner stone for a virtual model-ice tank by investigating and defining the mechanical behavior of the model-scale ice. Model-scale ice is a surrogate material which scales the most relevant properties of full-scale ice. A fully functioning, full-scale ice simulation environment is preferable compared to a numerical ice tank. Such environments for full-scale show reasonable agreements with some measurements, but not for all (e.g. Valanto, 2001; Derradji-Aouat, 2010). In full-scale the ship performance is rarely combined with detailed ice property measurements, and most ice property measurements are conducted stationarily and their variation along the ship's voyage is not captured as, for example, in Suominen et al. (2013). In model-scale, however, both the ice properties of the entire ice sheet as well as the ship performance parameters (e.g. resistance, thrust, torque) can be accurately measured. Consequently, for the validation of a numerical ice tank that relies on physical parameters, data of higher quantity and quality are at hand than for full-scale simulators. This would allow for one to assess the inter-dependence between ship performance and ice properties and eventually shift some tests in the future to the computer. Furthermore, a validated numerical ice tank offers the possibility to replace properties that do not scale well with target values based on full-scale measurements. This would offer two

additional possibilities: one is to assess the impact of scale effects related to ice properties and the second is to create a simulation environment that performs better than the actual tank and may lead to a well functioning full-scale simulation environment. Ultimately, a virtual ice tank provides a deeper insight into the model-scale ice itself and may provide starting-points for further developments of the physical tank.

A. Tabulated Data of Experiments

Table A.0.1. Tabulated values of the experiments conducted and presented in PI and PII with test numbers equivalent to the publications. The labels of the test numbers are equivalent to the ones used in PI, PII and PIII.

Compressive experiments (all specimens are of 25 mm length)					
Test	Maximum force [N]	Displacement at failure [mm]	Average slope [N/mm]	Ice thickness [mm]	Specimen width [mm]
C 31	57.2	4.1	13.9	27	26
C 32	49.7	3.8	13.1	25	26
C 33	67.3	5.7	11.8	25	26
C 34	78.1	6.5	12.0	26	25
C 35	69.4	5.3	13.1	25	25
C 36	38.4	2.9	13.3	27	25
C 37	47.9	3.2	15.0	26	26
C 38	67.3	4.2	16.0	26	25
C 39	47.6	3.1	15.4	26	25
Tensile experiments					
Test	Maximum force [N]	Displacement at failure [mm]	Average slope [N/mm]	Ice thickness [mm]	Thinnest width [mm]
T 31	42.4	3.7	11.5	25	25
T 32	7.0	1.0	7.0	26	25
T 33	22.0	1.9	11.6	25	25
T 35	21.3	2.1	10.1	25	25
T 36	30.0	3.0	10.0	24	25
T 38	15.4	1.5	10.3	24	25
T 39	20.2	1.9	10.6	24	25

Table A.0.2. Tabulated values of the experiments conducted and presented in PI and PIII. The labels of the test numbers are equivalent to the ones used in PI, PII and PIII.

Cantilever beam experiments			
Test	Maximum force [N]	Displacement at failure [mm]	Average slope [N/mm]
IB 1	2.64	4.7	0.6
IB 2	2.74	5.4	0.5
IB 3	2.13	4.0	0.5
IB 4	2.55	5.0	0.5
IB 5	2.41	5.5	0.4
IB 6	2.19	4.9	0.4
IB 7	3.06	6.0	0.5
IB 8	2.29	4.3	0.5

Table A.0.3. Data of the experimental cantilever beam tests including average values. The beam length, l, is the difference between the beam length after failure, l_b, and the distance between plunger and beam tip, d_p. The dimensions are ice thickness, h, and beam width, b. The maximum force is F, and Δ_{tot} is the total uncertainty in of σ_b due to measurement accuracies (PIII).

Test	h [mm]	b [mm]	l_b [mm]	d_p [mm]	l [mm]	F [N]	σ_b [kPa]	Δ_{tot} [kPa]
IB 1	26	58	173	19	154	2.64	62.13	4.96
IB 2	27	58	170	25	145	2.74	56.47	4.37
IB 3	24	59	165	19.5	145.5	2.13	54.78	4.72
IB 4	26	58	175	17	158	2.55	61.55	4.91
IB 5	25	60	174	15	159	2.41	61.26	5.06
IB 6	27	56	172	19	153	2.19	49.36	3.82
IB 7	26	56.5	177	17	160	3.06	76.88	6.14
IB 8	27	59	173	15	158	2.29	50.40	3.88
Average:							59.10	4.73

B. Material Model Parameters

Table B.0.1. Material parameters of the Lemaitre damage law in LS DYNA, see also LS-DYNA (2013).

Parameter	Function	Origin
Elastic modulus	Definition of initial stress-strain relationship until yielding	Experiment (infinite plate on elastic foundation, ITTC (2002))
Yield strength	Stress, which marks the end of the elastic regime and the beginning of the plastic regime	Experiments and FE simulations
Mass density	Defines the density of the model-ice grains	Estimate $917 kg/m^3$
Poisson's ratio		Literature and tank standard 0.3 (Riska et al., 1998)
Hardening modulus	Isotropic hardening modulus, which defined the stress-strain relationship after yielding	Based on compliance of numerical and experimental force-displacement curves
IDAMAGE	IDAMAGE = 1, Activation of damage	LS-DYNA (2013)
IDS	IDS = 1, Output of damaged stresses	LS-DYNA (2013)
IDEP	IDEP = 1, Damaged plastic strain is accumulated	LS-DYNA (2013)
EPSD	EPSD = 0, Damage threshold value, which starts accumulating immediately after yielding	Best estimate, LS-DYNA (2013)
S	Damage resistance parameter S = 25 Pa, default value = yield strength / 200	Best estimate
t_d	Damage exponent $t_d = 2$, default value = 1	Best estimate
d_c	Critical damage value at which the element is deleted	Compliance FE simulations with experiments

C. FE Stress Plots

In all sections the stresses are plotted at four marked instances d1 to d4. In addition to the highest stress in some cases also the visible most dominant stress color is stated.

C.1 Functionally Graded Cantilever Beam [PIII]

The four instances are at the beginning of the loading process, at constant force increase (d2), and the highest load (d3) and at failure (d4).

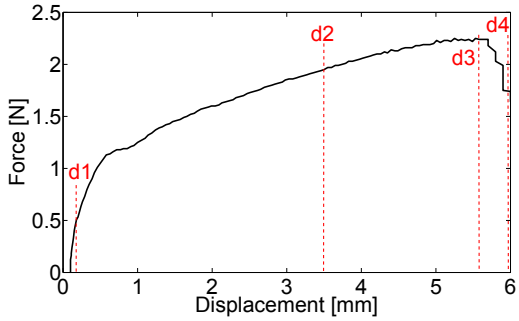

a Force-displacement curve of a simulated cantilever beam simulation

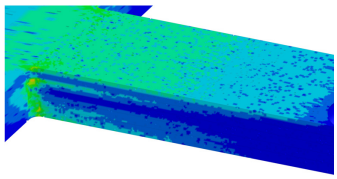

b d1, at load initiation, $\sigma_{vM,max} = 3.0 \cdot 10^4 Pa$, $\sigma_{vM,yellow} = 2.4 \cdot 10^4 Pa$

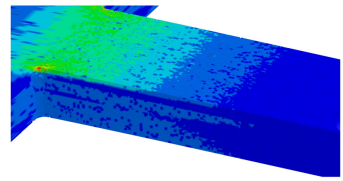

c d2, in the loading progress, $\sigma_{vM,max} = 1.9 \cdot 10^5 Pa$

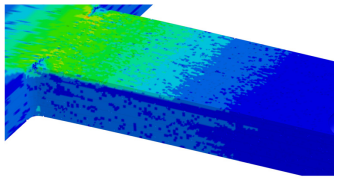

d d3, at maximum load, $\sigma_{vM,max} = 2.0 \cdot 10^5 Pa$

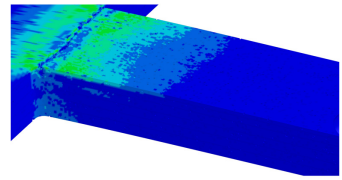

e d4, after failure, $\sigma_{vM,max} = 2.4 \cdot 10^5 Pa$, $\sigma_{vM,green} = 1.5 \cdot 10^5 Pa$

Figure C.1.1. von Mises stress distribution in a cantilever beam at different displacements.

C.2 Numerical Tensile Test with Constant Properties Through-Thickness [PII]

The four instances are at yielding (d1), at constant force increase (d2), and the highest load (d3) and at failure (d4).

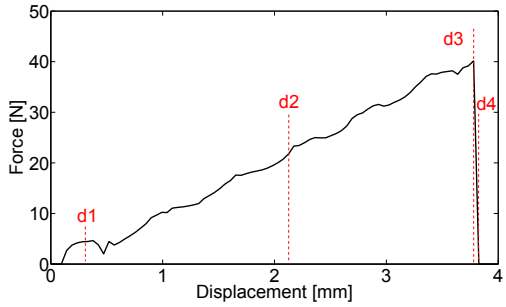

a Force-displacement curve of a simulated tensile specimen

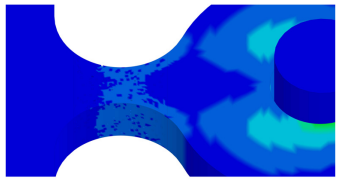

b d1, after load application, $\sigma_{vM,max} = 1.1 \cdot 10^4 Pa$, $\sigma_{vM,\ light\ blue} = 2.2 \cdot 10^3 Pa$

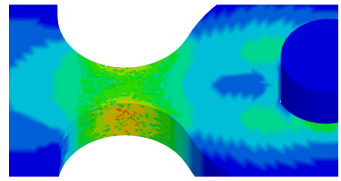

c d2, in loading progress, $\sigma_{vM,max} = 5.9 \cdot 10^4 Pa$

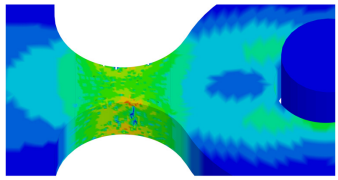

d d3, at maximum load, $\sigma_{vM,max} = 1.1 \cdot 10^5 Pa$

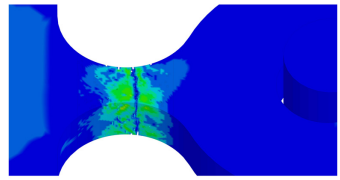

e d4, after failure, $\sigma_{vM,max} = 7.2 \cdot 10^4 Pa$, $\sigma_{vM,green} = 4.3 \cdot 10^4 Pa$

Figure C.2.1. von Mises stress distribution in a tensile specimen at different displacements.

C.3 Numerical Compressive Test with Constant Properties Through-Thickness [PII]

The four instances at first contact (d1), at constant force increase (d2), and the highest load (d3) and at failure (d4). The numerical specimen is shown in front and top view.

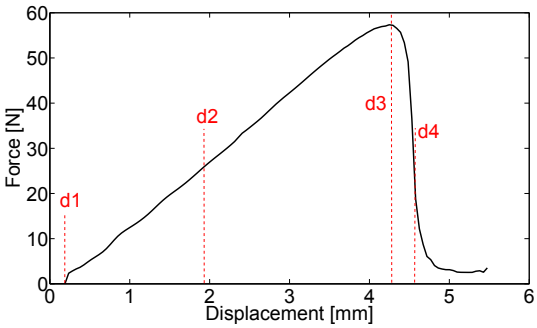

Figure C.3.1. Force-displacement curve of a simulated compressive specimen.

a Top-view on the specimen

b Front-view on the specimen impact face

Figure C.3.2. von Mises stress distribution at displacement d1, the initial impact, $\sigma_{vM,max} = 4.5 \cdot 10^3$ Pa.

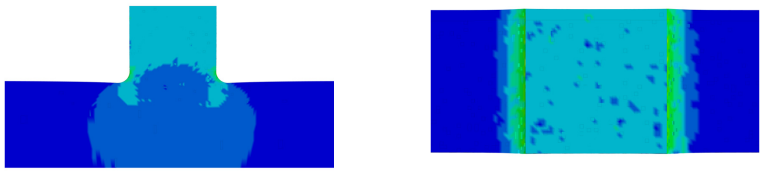

a Top-view on the specimen

b Front-view on the specimen impact face

Figure C.3.3. von Mises stress distribution at displacement d2, the loading process, $\sigma_{vM,max} = 1.4 \cdot 10^5 Pa$, $\sigma_{vM,green} = 1.0 \cdot 10^5 Pa$.

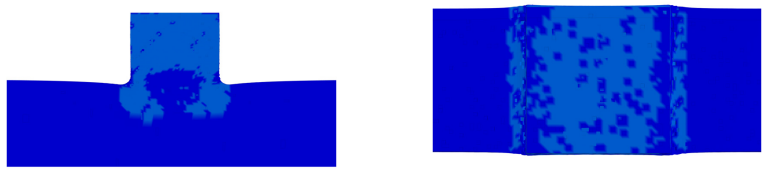

a Top-view on the specimen

b Front-view on the specimen impact face

Figure C.3.4. von Mises stress distribution at displacement d3, maximum load, $\sigma_{vM,max} = 6.3 \cdot 10^5 Pa$, $\sigma_{vM,lightblue} = 1.3 \cdot 10^5 Pa$.

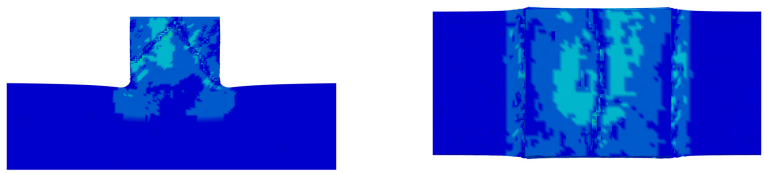

a Top-view on the specimen

b Front-view on the specimen impact face

Figure C.3.5. von Mises stress distribution at displacement d4, developed failure pattern, $\sigma_{vM,max} = 2.96 \cdot 10^5 Pa$, $\sigma_{vM,turquoise} = 8.9 \cdot 10^4 Pa$.

Errata

PI: On page 79 the yield strength is stated erroneously as ”0. kPa”, which must be ”0.5 kPa”

PII: On page 54 in Equation 1 the symbol Y must be the damage release rate, which has the same symbol as the yield strength

PIII: Table 6 on page 101 contains erroneous dc values, for which must be replaced with values of Table 5.1

PIV: In Figure 4 the elastic modulus E = 117 is a misprint and must be E = 110. In consequence also E/σ_b must be 1864 instead of 1983.

Bibliography

19906, I. (2010). Petroleum and natural gas industries - arctic offshore structures. Technical report.

Anderson, D. and Weeks, W. (1958). A theoretical analysis of sea-ice strength. *Transactions, American Geophisical Union*, 39(4):632 – 640.

Ashby, M. and Duval, P. (1985). The creep of polycrystalline ice. *Cold Regions Science and Technology*, 11(3):285–300.

Atkins, A. (1975). Icebreaking modeling. *Journal of Ship Research*, 19(1):40 – 43.

Atkins, A. G. and Caddell, R. M. (1974). The laws of similitude and crack propagation. *International Journal of Mechanical Sciences*, 16(8):541–548.

Bürgmann, R. and Dresen, G. (2008). Rheology of the lower crust and upper mantle: Evidence from rock mechanics, geodesy, and field observations. *Annual Review of Earth and Planetary Sciences*, 36:531–567.

Cammaert, A. and Muggeridge, D. (1988). *Ice interaction with offshore structures*. Van Nostrand Reinhold, U.S., New York (NY).

Chaboche, J. (1987). Continuum damage mechanics: Present state and future trends. *Nuclear Engineering and Design*, 105:19–33.

Cheng, H. (1968). Performance comparisons of marine vehicles. Meeting of the New York Metropolitan Section of The Society of Naval Architects and Marine Engineers (SNAME), New York.

Das, J., Polic, D., Ehlers, S., and Amdahl, J. (2014). Numerical simulation of an ice beam in four-point bending using sph. volume 10. Proceedings of the International Conference on Offshore Mechanics and Arctic Engineering (OMAE), San Francisco.

Dempsey, J., Palmer, A., and Sodhi, D. (2001). High pressure zone formation during compressive ice failure. *Engineering Fracture Mechanics*, 68(17-18):1961–1974.

Derradji-Aouat, A. (2003). Multi-surface failure criterion for saline ice in the brittle regime. *Cold regions science and technology*, 36:47–70.

Derradji-Aouat, A. (2010). Critical roles of constitutive laws and numerical models in the design and development of arctic offshore installations. pages 353–360. International Conference and Exhibition on Performance of Ships and Structures in Ice (ICETECH), Anchorage.

Derradji-Aouat, A., Sinha, N., and Evgin, E. (2000). Mathematical modelling of monotonic and cyclic behaviour of fresh water columnar grained s-2 ice. *Cold Regions Science and Technology*, 31(1):59–81.

Ehlers, S., Cheng, F., Kühnlein, W., Jordaan, I., Kujala, P., Luo, Y., Riska, K., Sirkar, J., Oh, Y., Terai, K., and Valkonen, J. (2015). Arctic technology. Technical report, 19th INTERNATIONAL SHIP AND OFFSHORE STRUCTURES CONGRESS.

Ehlers, S. and Kujala, P. (2014). Optimization-based material parameter identification for the numerical simulation of sea ice in four-point bending. *Proceedings of the Institution of Mechanical Engineers Part M: Journal of Engineering for the Maritime Environment*, 228:70 – 80.

Enkvist, E. (1972). On the ice resistance encountered by ships operating in the continuous mode of ice breaking. Technical report, The Swedish Academy of Engineering Sciences in Finland.

Enkvist, E. (1983). A survey of experimental indicators of the relation between submersion and breaking components of level ice resistance to ship. volume 1. Conference on Port and Ocean Engineering under Arctic Conditions (POAC), Helsinki.

Enkvist, E. (1990). Physical modelling of icebreaking ships in fine-grain model ice. pages 15 – 42. International Association for Hydro-Environment Engineering and Research (IAHR) Ice Symposium, Espoo.

Enkvist, E. and Mäkinen, S. (1984). A fine-grain model ice. IAHR Ice Symposium Hamburg.

Enkvist, E., Varsta, P., and Riska, K. (1979). Ship-ice interaction. pages 977–1002. Conference on Port and Ocean Engineering Under Arctic Conditions (POAC), Trondheim.

Ettema, R., Stern, F., and Lazaro, J. (1987). Dynamics of contineous-mode icebreaking by a polar-class icebreaker hull. Technical Report 24, United States Department of Transportation and University of Iowa.

Ettema, R., Stern, F., and Lazaro, J. (1989). Dynamics of continuous-mode icebreaking by a polar-class hull. part 1. mean response. *Journal of Ship Research*, 33(2):115–134.

Evers, K.-U. and Jochman, P. (1993). An advanced technique to improve the mechanical properties of model ice developed at the hsv a ice tank. Conference on Port and Ocean Engineering under Arctic Conditions (POAC), Hamburg.

Glen, J. W. (1955). The creep of polycrystalline ice. *Proceedings of the Royal Society of London A: Mathematical, Physical and Engineering Sciences*, 228(1175):519–538.

Golan, O., Arbel, A., Eliezer, D., and Moreno, D. (1996). The applicability of norton's creep power law and its modified version to a single-crystal superalloy type cmsx-2. *Materials Science and Engineering: A*, 216:125 – 130.

Gold, L. (1970). *THE FAILURE PROCESS IN COLUMNAR-GRAINED ICE*. PhD thesis, McGill University, Montreal.

Goldstein, R. and Osipenko, N. (1993). Fracture mechanics in modeling of icebreaking capability of ships. *Journal of Cold Regions Engineering*, 7(2):33–43.

Gow, A. and Ueda, H. (1989). Structure and temperature dependence of the flexural strength properties of laboratory freshwater ice sheets. *Cold Regions Science and Technology*, 16:249 – 246.

Grochowalski, S. and Hermanski, G. (2011). Ship resistance and propulsion in ice-covered waters: An experimental study. volume 119, pages 67–92. Transactions - Society of Naval Architects and Marine Engineers (SNAME), Houston.

Gürtner, A. (2009). *Experimental and Numerical Investigations of Ice-Structure Interaction*. PhD thesis, Norwegian University of Science and Technology (NTNU).

Hawkes, I. and Mellor, M. (1972). Deformation and fracture of ice under uniaxial stress. *Journal of Glaciology*, 11:103–131.

International Maritime Organization (2013). IMO marine environment protection committee 65th session pushes forward with energy-efficiency implementation. IMO-MEPC65, `http://www.imo.org/mediacentre/pressbriefings/pages/18-mepc65ends.aspx`.

ITTC (2002). Ice property measurements, 7.5-02-04-02. `http://ittc.sname.org`.

ITTC (2005). Experimental uncertainty analysis for ship resistance in ice tank testing, 7.5-02-04-02.5. `http://ittc.sname.org`.

ITTC (2014). Ice property measurements, 7.5-02-04-02. `http://ittc.sname.org`.

Jalonen, R. and Ilves, L. (1990). Experience with a chemically-doped fine-grained model ice. volume 2, pages 639 – 651. International Association for Hydro-Environment Engineering and Research (IAHR) Ice Symposium, Espoo.

Johnston, M., Croasdale, K., and Jordaan, I. (1998). Localized pressures during ice-structure interaction: relevance to design criteria. *Cold Regions Science and Technology*, 27(2):105–117.

Jones, S. (1982). The confined compressive strength of polycrystalline ice. *Journal of Glaciology*, 28(98):171–177.

Jordaan, I. (2001). Mechanics of ice-structure interaction. *Engineering Fracture Mechanics*, 68:1923–1960.

Jordaan, I., Matskevitch, D., and Meglis, I. (1999). Disintegration of ice under fast compressive loading. *International Journal of Fracture*, 97(1-4):279–300.

Jordaan, I., Taylor, R., and Derradji-Aouat, A. (2012). Scaling of flexural and compressive ice failure. volume 6, pages 589–595.

Karr, D. and Das, S. (1983). Ice strength in brittle and ductile failure modes. *Journal of Structural Engineering*, (109):2802 – 2811.

Keinonen, A., Browne, R., and Revill, C. (1991). Icebreaker design synthesis phase 2 analysis of contemporary icebreaker performance. Technical Report TP 10923 E, Transport Canada.

Kerr, A. and Palmer, W. (1972). The deformations and stresses in floating ice plates. *Acta Mechanica*, 15:57–72.

Kolari, K. (2007). *Damage mechanics model for brittle failure of transversely isotropic solids, Finite element implementation*. PhD thesis, Helsinki University of Technology.

Kolari, K., Kuutti, J., and Kurkela, J. (2009). Fe-simulation of continuous ice failure based on model update technique. Number POAC09-94. Conference on port and ocean engineering under arctic conditions (POAC), Luleå.

Kärmäräinen, J. (1993). Evaluation of ship ice resistance calculation methods. Licentiate thesis at Helsinki University of Technology.

Kärmäräinen, J. (2007). *THEORETICAL INVESTIGATION ON THE EFFECT OF FLUID FLOW BETWEEN THE HULL OF A SHIP AND ICE FLOES ON ICE RESISTANCE IN LEVEL ICE*. PhD thesis, HELSINKI UNIVERSITY OF TECHNOLOGY.

Krupina, N. A. and Kubyshkin, N. (2007). Flexural strength of drifting level first-year ice in barents sea. *Journal of Offshore and Polar Engineering*, 17:169 – 175.

Kujala, P. and Riska, K. (2010). *Talvimerenkulku*. Number TKK-AM-13. Helsinki University of Technology.

Kujala, P., Riska, K., Varsta, P., Koskivaara, R., and Nyman, T. (1990). Results from in situ four point bending tests with baltic sea ice. pages 261 – 278. International Association for Hydro-Environment Engineering and Research (IAHR) Ice Symposium, Espoo.

Le Gac, H. and Duval, P. (1979). *Physics and Mechanics of Ice*, chapter Constitutive Relations for the Non Elastic Deformation of Polycrystalline Ice, pages 51 – 59. Springer Verlag.

Lemaitre, J. and Desmorat, R. (1992). *Engineering Damage Mechanics*. Springer Verlag.

Li, Z. and Riska, K. (2002). Index for estimating physical and mechanical parameters of model ice. *Journal of Cold Regions Engineering*, 16(2):72–82.

Lindqvist, G. (1989). A straightforward method for calculation of ice resistance of ships. volume 2, pages 722–735. Conference on port and ocean engineering under arctic conditions (POAC), Luleå.

LS-DYNA (2013). *KEYWORD USER'S MANUAL*. LS-DYNA, 7 edition.

McKenna, R. (1992). Discrete modelling of grain scale deformation mechanisms for ice in compression. pages 152 – 163. International Association for Hydro-Environment Engineering and Research (IAHR) Ice Symposium, Banff.

Moore, P., Jordaan, I., and Taylor, R. (2013). Explicit finite element analysis of compressive ice failure using damage mechanics. Conference on Port and Ocean Engineering under Arctic Conditions (POAC), Espoo.

Moores, C., Veitch, B., Bose, N., Jones, S. J., and Bugden, A. (2001). EFFECTS OF STRAIN RATE AND TEMPERATURE ON THE UNIAXIAL COMPRESSIVE STRENGTH OF EG/AD/S CD MODEL ICE. volume 3. Conference on Port and Ocean Engineering under Arctic Conditions (POAC), Ottawa.

Myland, D. and Ehlers, S. (2014). Theoretical investigation on ice resistance prediction methods for ships in level ice. In *Volume 10: Polar and Arctic Science and Technology*, volume 10. Proceedings of the International Conference on Offshore Mechanics and Arctic Engineering (OMAE), San Francisco.

Nyman, T. (1986). On the ice-breaking component in level ice resistance. IAHR Symposium on Ice, Iowa City.

Palmer, A. (2008). *Dimensional Analysis and Intelligent Experimentation*. World Scientific Publishing Company. ISBN 10: 9812708197.

Palmer, A., Dempsey, J., and Masterson, D. (2009). A revised ice pressure-area curve and a fracture mechanics explanation. *Cold Regions Science and Technology*, 56(2-3):73 – 76.

Palmer, A. C., Goodman, D. J., Ashby, M. F., Evans, A. G., Hutchinson, J. W., , and Ponter, A. R. S. (1983). Fracture and its role in determining ice forces on offshore structures. *Annals ofGlaciolog*, pages 216 – 221.

Petrich, C. and Eicken, H. (2009). *Sea Ice*, chapter Growth, Structure and Properties of Sea Ice. Wiley-Blackwell, Oxford, UK.

Poznyak, I. I. and Ionov, B. P. (1981). The disvision of ice breaker resistance into components. In *Sixth Ship Technology and Research (STAR) Symposium, Ottawa*. Society of Naval Architects and Marine Engineers (SNAME).

Reddy, J. (2011). Microstructure-dependent couple stress theories of functionally graded beams. *Journal of the Mechanics and Physics of Solids*, 59(11):2382–2399.

Richter-Menge, J. and Jones, K. (1993). The tensile strength of first-year sea ice. *Journal of Glaciology*, 39(133):609–618.

Riska, K. (2010). *DESIGN OF ICE BREAKING SHIPS*. The Auspices of the UNESCO, Eolss Publishers, Oxford ,UK.

Riska, K., Jalonen, R., Veitch, B., Nortala-Hoikkanen, A., and Wilkman, G. (1994). Assessment of ice model testing techniques. International Conference and Exhibition on Performance of Ships and Structures in Ice (ICETECH), Calgary.

Riska, K., Wilhelmson, M., Englund, K., and Leiviskä, T. (1998). Performance of merchant vessels in ice in the baltic. Technical report, Finnish Maritime Administration.

R.S., T. and I.J., J. (2015). Probabilistic fracture mechanics analysis of spalling during edge indentation in ice. *Engineering Fracture Mechanics*, 134:242–266. cited By 4.

Sames, P., Papanikolaou, A., Harries, S., Coyne, K., Zaraphonitis, G., and Tillig, F. (2011). Best plus - better economics with safer tankers. volume 119, pages 314–329. Transactions - Society of Naval Architects and Marine Engineers.

Sanderson, T. (1988). *Ice mechanics - risks to offshore structures*. Graham & Trotman.

Schulson, E. (1999). The structure and mechanical behavior of ice. *JOM - Journal of Materials*, 51(2):21–27. cited By 0.

Schulson, E. and Duval, P. (2009). *Creep and fracture of ice*. Cambridge University Press,, Cambridge, UK ;.

Schwarz, J. (1977). New developments in modeling ice problems. pages 45 – 61. Conference on port and ocean engineering under arctic conditions (POAC), St. John's.

Schwarz, J. (1985). Physical modeling techniques for offshore structures in ice. volume 3, pages 1113 – 1131. Conference on port and ocean engineering under arctic conditions (POAC), Narssarssuaq.

Åse, E. (2013). Experimental and numerical investigations of cantilever beam tests in floating ice covers. Master's thesis, Norwegian University of Science and Technology.

Shoji, A. and Higashi, A. (1978). A deformation mechanism map of ice. *Journal of Glaciology*, 21(85):419 – 427.

Sinha, N. (1978a). Rheology of columnar-grained ice. *Experimental Mechanics*, 18(12):464–470.

Sinha, N. (1978b). Short-term rheology of polycrystalline ice. *Journal of Glaciology*, 21(85):457 – 473.

Sinha, N. (1982). Constant strain- and stress-rate compressive strength of columnar-grained ice. *Journal of Materials Science*, 17(3):785–802.

Sinha, N. (1983). Field tests on rate sensitivity of vertical strength and deformation of first-year columnar-grained sea ice. volume 1, pages 231–242. VTT Symposium (Valtion Teknillinen Tutkimuskeskus).

Stone, B., Jordaan, I., Jones, S., and McKenna, R. (1989). Damage of isotropic polycrystalline ice under moderate confining pressures. volume 1, pages 408 – 419. International Conference on Port and Ocean Engineering under Arctic Conditions (POAC), Luleå.

Su, B., Riska, K., and Moan, T. (2010). A numerical method for the prediction of ship performance in level ice. *Cold Regions Science and Technology*, 60(3):177–188. cited By 39.

Suominen, M., Karhunen, J., Bekker, A., Kujala, P., Elo, M., von Bock und Polach, R., Enlund, H., and Saarinen, S. (2013). Full-scale measurements on board psrv s.a. agulhas ii in the baltic sea. Conference on port and ocean engineering under arctic conditions (POAC), Espoo.

Svec, O., Thompson, J., and Frederking, R. (1985). Stress concentrations in the root of an ice cover cantilever: Model tests and theory. *Cold Regions Science and Technology*, 11(1):63 – 73.

Tatinclaux, J.-C. P. (1988). Ship model testing in level ice: An overview. Technical Report CRREL Report 88-15, U.S. Army Corps of Engineers, Cold Regions Research and Engineering Laboratory (CRREL).

Timco, G. (1981a). Flexural strength of ice grown from chemically impure melts. *Cold Regions Science and Technology*, 4:81 – 92.

Timco, G. and Weeks, W. (2010). A review of the engineering properties of sea ice. *Cold Regions Science and Technology*, 60(2):107 – 129.

Timco, G. W. (1981b). On the test methods for model ice. *Cold Regions Science and Technology*, 4:269 – 274.

Valanto, P. (1997). On the icebreaking forces and resistance of a ship advancing in level ice. In *Proceedings of the International Conference on Offshore Mechanics and Arctic Engineering - OMAE*, volume 4, pages 63–71. Proceedings of the International Conference on Offshore Mechanics and Arctic Engineering (OMAE), Yokohama.

Valanto, P. (2001). The resistance of ships in level ice. *SNAME Transactions*, 119:53–83.

Valkonen, J., Izumiyama, K., and Kujala, P. (2007). Measuring of ice induced pressures and loads on ships in model scale. volume 2, pages 1206–1213. 10th International Symposium on Practical Design of Ships and other Floating Structures (PRADS), Houston.

Vance, G. (1975). A scaling system for vessels modelled in ice. The Society of Naval Architects and Marine Engineers (SNAME) Ice Tech Symposium, Montreal.

Vance, G. (1980). Analysis of the performance of a 140 great lakes icebreaker: USCGC Katmai Bay. Technical Report CRREL report 80-8, U.S. Army Corps of Engineers, Cold Regions Research and Engineering Laboratory (CRREL).

Varsta, P. (1983). *On the mechanics of ice load on ships in level ice in the Baltic Sea*. PhD thesis, Helsinki University of Technology.

von Bock und Polach, R. (2005). Sea ice characteristics and its consequences on model testing. Master's thesis, Technical University of Berlin.

von Bock und Polach, R. (2010). Impact of heave and pitch motions on ships in ice. *20th IAHR International Symposium on Ice*, (IAHR2010-101).

von Bock und Polach, R. and Ehlers, S. (2011). Heave and pitch motions of a ship in model ice: An experimental study on ship resistance and ice breaking pattern. *Cold Regions Science and Technology*, 68(1-2):49–59.

von Bock und Polach, R., Ehlers, S., and Erikstad, S. (2014). A decision-based design approach for ships operating in open water and ice. *Journal of Ship Production and Design*, 30(1 - 11).

von Bock und Polach, R., Tõns, T., and Erceg, S. (2015). Ice resistance calculation methods and their economic impact on ship design. Number OMAE2015-41342. Proceedings of the International Conference on Offshore Mechanics and Arctic Engineering (OMAE), St. John's.

Weeks, W. and Assur, A. (1967). The mechanical properties of sea ice. Technical Report II - C3, U.S. Army Corps of Engineers, Cold Regions Research and Engineering Laboratory (CRREL).

Wegner, K. (2011). Model ice property measurements for fe-simulations. Master's thesis, Technical University Hamburg-Harburg.

Weibull, W. (1939). *A Statistical Theory of the Strength of Materials.* Number 151.

Wilkman, G. (2014). A short history of ice model tests in finland. Number ICETECH14-164-RF. International Conference and Exhibition on Performance of Ships and Structures in Ice (ICETECH), Banff.

Wilkman, G., Forsén, A.-C., and Mattsson, T. (2010). Recent advancements in ice model testing at aker arctic. Number IAHR-137. International Association for Hydro-Environment Engineering and Research (IAHR) Ice Symposium, Lahti.

Yamaguchi, H., Suzuki, Y., and Izumiyama, K. (1997). Influence of the bow shape on ice breaking resistance in low speed range. *The 14th international conference on port and ocean engineering under Arctic conditions Joint POAC97 and 16th OMAE.*

Yamaguchi, H., Suzuki, Y., and Izumiyama, K. (1999). Influence of the bow shape on ice breaking resistance in high speed range. *The 18th international conference on offshore mechanics and arctic engineering -OMAE99.*

Zahn, P. and Philips, L. (1987). Towed resistance trials in ice of the uscgc mobile bay. Technical Report 1252C-2, Arctec Engineering Inc.

Zufelt, J. and Ettema, R. (1996). Model ice properties. Technical Report CRREL Report 96-1, U.S. Army Corps of Engineers, Cold Regions Research and Engineering Laboratory (CRREL).

The research presented in this thesis investigates the mechanical behavior of model-scale ice. A numerical model is built that can reproduce conducted experiments in compression, tension and bending. On this basis, an assessment of the ability of model-scale ice to scale the mechanical behavior of sea ice is made. The conducted research is to be seen in the context of ship-ice interactions.

Aalto-DD 98/2016

NTNU
Norwegian University of Science and Technology

ISBN 978-952-60-6822-0 (printed)
ISBN 978-952-60-6823-7 (pdf)
ISSN-L 1799-4934
ISSN 1799-4934 (printed)
ISSN 1799-4942 (pdf)

Aalto University
School of Engineering
Applied Mechanics
www.aalto.fi